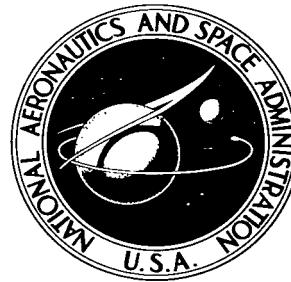# NASA TECHNICAL NOTE

NASA TN D-3578

c. 1

NASA TN D-3578

ANALYSIS OF THE LINEARIZED SUPERSONIC FLOW ABOUT POINTED BODIES OF REVOLUTION BY THE METHOD OF CHARACTERISTICS

by Alan D. Sherer

George C. Marshall Space Flight Center
Huntsville, Ala.

NASA TN D-3578

ANALYSIS OF THE LINEARIZED SUPERSONIC FLOW ABOUT POINTED

BODIES OF REVOLUTION BY THE METHOD OF CHARACTERISTICS

By Alan D. Sherer*

George C. Marshall Space Flight Center
Huntsville, Ala.

*Lockheed Missiles and Space Company, Huntsville Research and Engineering Center, Huntsville, Ala.

NATIONAL AERONAUTICS AND SPACE ADMINISTRATION

TABLE OF CONTENTS

LIST OF ILLUSTRATIONS

LIST OF ILLUSTRATIONS (Cont'd)

LIST OF ILLUSTRATIONS (Cont'd)

LIST OF ILLUSTRATIONS (Concluded)

LIST OF SYMBOLS

Symbol	Definition
Φ	velocity potential
u, v, w,	velocity components in x, r, ψ - directions
ξ, η	characteristic coordinates: left and right running Mach lines, respectively
M_∞	freestream Mach number
α	angle of attack
μ	Mach angle
C_p	pressure coefficient
ϵ	body fineness ratio
L	body length
U_∞	velocity of freestream
S(L)	cross-sectional area of body
C_M	moment coefficient
C_N	normal force coefficient
C_{M_α}	moment force coefficient slope
C_{N_α}	normal force coefficient slope
$\dfrac{d(C_{N_\alpha})}{dx}$	local normal force variation
h(x)	body contour

ANALYSIS OF THE LINEARIZED SUPERSONIC FLOW ABOUT POINTED BODIES OF REVOLUTION BY THE METHOD OF CHARACTERISTICS

SUMMARY

The method of characteristics applicable to the linear potential equation governing the supersonic flow over bodies of revolution at zero and small angles of attack is presented. For axisymmetric flow the equations used are those derived by Sauer and Heinz, whereas for flow due to angle of attack the equations are those derived by Oswatitsch and Erdmann. This analysis investigates the limits of applicability of these methods. The flow field computation was programmed in Fortran IV to be used for computing the axisymmetric and angle of attack flow fields about convex and concave parabolic ogives and cone-cylinder bodies of various body fineness ratios at low supersonic Mach numbers. The results of these computations were compared with J. L. Sims' exact method of characteristics, the linear theory of Reference 1, and, whenever available, with experimental data. It was found that these methods are applicable to flow fields where the hypersonic similarity parameter, $M_\infty \, \epsilon$, is less than about 0.6.

INTRODUCTION

The linearization of the potential equation for supersonic flow about a body of revolution rests on the assumption that the disturbances produced in the flow by such a body are everywhere small. The solution of the potential equation may be obtained by either the method of singularities or the method of characteristics. The application of singularity methods to the present problem is well documented in the literature having originated with Von Karman and Moore [2] for axial flow, and Tsien [3] for bodies at angle of attack. The method of characteristics as applied to the linearized potential equation is not very well known, especially in this country.

For flow fields where the potential equation can be linearized, there are several advantages in using linearized methods as opposed to exact methods. The speed of the linear methods and the simplicity of the equations involved are the primary advantages. Also, in the case of flow about cone-cylinder bodies, an important consideration is the ease with which the solution at the expansion corner may be obtained. In this situation, the exact method of characteristics involves a Prandtl-Meyer calculation in order to treat the flow field caused by the body slope discontinuity. In the linearized method of characteristics, the

flow field calculation at the expansion corner is treated by the use of a "double" characteristic reflected from the corner.

The linearized method of characteristics which is considered in this analysis is that of Sauer and Heinz [4] for axial flow, while for flow due to angle of attack the method is that of Oswatitsch and Erdmann [4]. The most important feature of these methods is that the particular combination of flow variables in the compatibility relations eliminates the singular behavior caused by the use of cylindrical coordinates so that these modified variables change quite slowly near the body. This in turn permits the use of a relatively large grid size which makes possible a very fast numerical calculation of the flow field.

The nondimensionalization of the quantities used in the following treatment, where starred (*) quantities are dimensional and unstarred quantities are dimensionless, is

$$\Phi = \frac{\Phi^*}{L^* \, U_\infty^*} \qquad\qquad x = \frac{x^*}{L^*}$$

$$u = \frac{u^*}{U_\infty^*} \qquad\qquad R(x) = \frac{R^* \, (x^*)}{L^*}$$

$$v = \frac{v^*}{U_\infty^*} \qquad\qquad \epsilon = \frac{R^* \, (L^*)}{L^*}$$

$$w = \frac{w^*}{U_\infty^*}$$

The cylindrical coordinate system $(x, \, r, \, \psi)$ used in the following treatment is affixed with the body so that the x-axis is coincident with the axis of symmetry of the body (Fig. 1).

TECHNICAL DISCUSSION

The Nature of the Procedure

We start with the linearized potential equation for supersonic flow

$$(M_\infty^2 - 1) \, \frac{\partial^2 \Phi}{\partial x^2} - \frac{\partial^2 \Phi}{\partial r^2} - \frac{1}{r^2} \, \frac{\partial^2 \Phi}{\partial \psi^2} - \frac{1}{r} \, \frac{\partial \Phi}{\partial r} = 0 . \tag{1}$$

2

With $G(x, r)$ as the perturbation potential of the axisymmetric part of the flow and $F(x, r)$ as the perturbation potential of the flow due to angle of attack, we may write as a solution of equation (1)

$$\Phi = \cos \alpha \, [x + G(x, r)] + \sin \alpha \cos \psi \; F(x, r) \; . \tag{2}$$

The velocity components in terms of the potential Φ are

$$u = \frac{\partial \Phi}{\partial x} \; , \quad v = \frac{\partial \Phi}{\partial r} \; , \quad w = \frac{1}{r} \frac{\partial \Phi}{\partial \psi} \; .$$

Taking the inclination in the plane $\psi = 0$, and introducing equation (2) into equation (1), we get for the axisymmetric part of the flow

$$(M_\infty^2 - 1) \frac{\partial^2 G}{\partial x^2} - \frac{\partial^2 G}{\partial r^2} - \frac{1}{r} \frac{\partial G}{\partial r} = 0, \tag{3}$$

and for flow due to angle of attack

$$(M_\infty^2 - 1) \frac{\partial^2 F}{\partial x^2} - \frac{\partial^2 F}{\partial r^2} - \frac{1}{r} \frac{\partial F}{\partial r} + \frac{1}{r^2} \; F = 0 \; . \tag{4}$$

The axisymmetric disturbance velocity components divided by $\cos \alpha$ are

$$u' = \frac{\partial G}{\partial x} \; , \qquad\qquad v' = \frac{\partial G}{\partial r}$$

and the angle-of-attack disturbance velocities divided by $\sin \alpha \cos \psi$ are

$$u'' = \frac{\partial F}{\partial x} \; , \qquad\qquad v'' = \frac{\partial F}{\partial r} \; .$$

To facilitate further derivation, the relations of equation (3) and (4) may be combined into a single relation

$$(M_\infty^2 - 1) \frac{\partial^2 \Phi}{\partial x^2} - \frac{\partial^2 \Phi}{\partial r^2} - \frac{1}{r} \frac{\partial \Phi}{\partial r} + \frac{\lambda}{r^2} \; \Phi = 0, \tag{5}$$

where

$$\Phi = G \text{ for } \lambda = 0$$

and

$$\Phi = F \quad \text{for } \lambda = 1.$$

The potential equation (5) can be written as

$$\beta^2 \frac{\partial u}{\partial x} - \frac{\partial v}{\partial r} - \frac{1}{r} v + \frac{\lambda}{r^2} \Phi = 0 \tag{6}$$

$$\frac{\partial u}{\partial r} - \frac{\partial v}{\partial x} = 0$$

where

$$\beta^2 = M_\infty^2 - 1, \qquad \frac{\partial \Phi}{\partial x} = u, \qquad \frac{\partial \Phi}{\partial r} = v.$$

This hyperbolic partial differential equation (for $M_\infty > 1$) has two families of characteristic curves ξ and η. The curves for $\xi = $ constant are referred to as left-running characteristic lines, while those for $\eta = $ constant are called right-running characteristic lines.

The following relations apply to these characteristic lines:

$$\xi = x - \beta r \qquad \text{(left-running lines)} \tag{7}$$

$$\eta = x + \beta r \qquad \text{(right-running lines)}.$$

From equations (1) through (7), the compatibility relations for axisymmetric flow may be obtained. These relations,

$$\frac{\partial(rv')}{\partial \xi} = - \beta r \frac{\partial u'}{\partial \xi} \tag{8a}$$

and

$$\frac{\partial(rv')}{\partial \eta} = \beta r \frac{\partial u'}{\partial \eta} \tag{8b}$$

are the fundamental relations on which the Sauer-Heinz linear characteristics method for axisymmetric supersonic flow is based. They are used to obtain the values of u' and v' along the characteristic lines described previously, which are just the Mach lines of the freestream.

4

The compatibility relations for flow due to angle of attack are obtained from equations (1) through (7) also. These relations

$$\frac{\partial}{\partial \xi} \left(v'' + \frac{F}{r} \right) = -\frac{\beta}{r} \frac{\partial (ru'')}{\partial \xi} \tag{9a}$$

and

$$\frac{\partial}{\partial \eta} \left(v'' + \frac{F}{r} \right) = \frac{\beta}{r} \frac{\partial (ru'')}{\partial \eta} , \tag{9b}$$

are the relations on which the Erdmann-Oswatitsch linear characteristics method for flow due to angle of attack is based. They are used to determine the values of ru'' and $v'' + \dfrac{F}{r}$ along the characteristic lines, i.e., the free-stream Mach lines.

To solve the linearized potential equation (1), it suffices to solve, in the case of axisymmetric flow, equations (8a) and (8b) for u' and v' and, in the case of flow due to angle of attack, equations (9a) and (9b) for u'' and v''. Knowing these values, any other desired flow property may be obtained at any point within the region of disturbed flow.

Calculation of the Flow Properties in the Field

To explain the calculation of the flow properties in the field, we will consider point 4 as an example (Fig. 1). The physical coordinates of the field points are obtained by solution of the left- and right-running characteristic lines simultaneously. Replacing equation (8a) by its finite difference form and applying it along the right-running characteristic line $\overline{3, 4}$ we obtain

$$(rv')_3 - (rv')_4 = -\beta r_\eta (u'_3 - u'_4). \tag{10a}$$

Similar application of equation (8b) along the left-running characteristic line $\overline{2, 4}$ yields

$$(rv')_2 - (rv')_4 = \beta r_\xi (u'_2 - u'_4) , \tag{10b}$$

where r_η is the average ordinate between the two points under consideration on the right-running characteristic line and r_ξ is the average ordinate between the two points under consideration on the left-running characteristic line.

5

Simultaneous solution of equations (10a) and (10b) yields for u'_4

$$u'_4 = \frac{(rv')_3 - (rv')_4 + \beta(r_\eta u'_3 + r_\xi u'_2)}{\beta(r_\xi + r_\eta)} \tag{11}$$

and for $(rv')_4$

$$(rv')_4 = \frac{r_\xi (rv')_3 + r_\eta (rv')_2 - \beta r_\xi r_\eta (u'_2 - u'_3)}{r_\xi + r_\eta} . \tag{12}$$

Equations (11) and (12) give the values of the zero angle-of-attack flow properties, u' and rv', at field point 4.

By the following identical procedure with equations (9a) and (9b), the relations which give the values of the angle-of-attack flow properties at point 4 may be obtained. These relations are

$$(ru'')_4 = \frac{r_\xi r_\eta \left[\left(v'' + \frac{F}{r} \right)_3 - \left(v'' + \frac{F}{r} \right)_2 \right] + \beta \left[r_\xi (ru'')_3 + r_\eta (ru'')_2 \right]}{\beta(r_\eta + r_\xi)} \tag{13}$$

and

$$\left(v'' + \frac{F}{r} \right)_4 = \frac{r_\eta \left(v'' + \frac{F}{r} \right)_3 + r_\xi \left(v'' + \frac{F}{r} \right)_2 - \beta \left[(ru'')_2 - (ru'')_3 \right]}{r_\eta + r_\xi} . \tag{14}$$

Equations (11), (12), (13), and (14) give the values of the flow properties at point 4 in terms of known values at points 2 and 3. The solutions of the other field points are obtained by a similar procedure.

Calculation of the Flow Properties at the Body

To explain the calculation of the flow properties at the body, we will consider point 5 (Fig. 1). The physical coordinates of the body point are obtained by simultaneous solution of the equation of the right-running characteristic line and equation of the body.

6

Consider a body contour given by $r = h(x)$ (Fig. 1). Then the flow direction Θ in the plane $\psi = 0$, with velocity components $u = \dfrac{\partial \Phi}{\partial x}$ and $v = \dfrac{\partial \Phi}{\partial r}$ in accordance with equation (1), is given by the relation

$$\tan \Theta = \frac{dh}{dx} = \frac{\dfrac{\partial \Phi}{\partial r}}{\dfrac{\partial \Phi}{\partial x}} = \frac{v' + v'' \tan \alpha}{1 + u' + u'' \tan \alpha} \ . \tag{15}$$

Hence, there follows the exact boundary condition for axisymmetric flow:

$$v'_5 = \left(\frac{dh}{dx}\right)_5 (1 + u'_5) \ . \tag{16}$$

Equation (16) inserted into equation (15) gives, after brief manipulation, the exact boundary conditions for flow at angle of attack:

$$v'' = u'' \frac{dh}{dx} \tag{17}$$

Applying equation (8a) along $\overline{4,5}$, as in the previous section, we obtain

$$(rv')_4 - (rv')_5 = -\beta r_\eta \ (u'_4 - u'_5) \ . \tag{18a}$$

Simultaneous solution of equations (16) and (18a) yields

$$u'_5 = \frac{\beta r_\eta \ u'_4 + (rv')_4 - r_5 \left(\dfrac{dh}{dx}\right)_5}{\beta r_\eta + r_5 \left(\dfrac{dh}{dx}\right)_5} \ . \tag{18b}$$

Equations (15) and (18b) give the values of the zero angle-of-attack flow properties at body point 5.

Application of equation (9a) along $\overline{4,5}$ yields

$$\left(v'' + \frac{F}{r}\right)_4 - \left(v'' + \frac{F}{r}\right)_5 = -\frac{\beta}{r_\eta} \left[(ru'')_4 - (ru'')_5\right] \ . \tag{19}$$

Equation (19) shows that, in order to determine the value of v" at the body, an explicit knowledge of F along the body is necessary. The differential of F is

$$dF(x, r) = \frac{\partial F}{\partial x} \, dx + \frac{\partial F}{\partial r} \, dr = u" \, dx + v" \, dr. \tag{20}$$

If the step size is taken sufficiently small, the wall elements $\Delta\ell$ (Fig. 1) can be considered straight lines, and we have

$$\Delta x = \cos \Theta \, \Delta\ell \qquad \text{and} \quad \Delta r = \sin \Theta \, \Delta\ell, \tag{21}$$

and from equation (17),

$$v" = u" \tan \Theta. \tag{22}$$

As stated previously, the primary advantage of this method is that it permits the use of a relatively large grid size. *The preceding restriction is not in contradiction with this fact since the method assumes that the rate of change in the slope of the body is small.*

Equations (21), which are difference equations, and equation (22) inserted into equation (20) yield

$$\Delta F \, (x, r) = \frac{u"}{\cos \Theta} \, \Delta\ell = u" \, \frac{\Delta\ell^2}{\Delta x} . \tag{23}$$

Application of equation 23 along the body segment $\overline{2,5}$ gives F at the new body point 5 in terms of known properties at the previous body point 2 and $u_5"$, which is still unknown:

$$F_5 = F_2 + \frac{1}{2} \, [u_2" + u_5"] \, \frac{\Delta\ell^2}{\Delta x} . \tag{24}$$

Combining equation (17) with equation (24) yields for $(v" + \frac{F}{r})$ at point 5

$$\left(v" + \frac{F}{r}\right)_5 = u_5"\left(\frac{dh}{dx}\right)_5 + \frac{F_2 + (u_2" + u_5") \, \frac{\Delta\ell^2}{2\Delta x}}{r_5} , \tag{25}$$

and equation (25) inserted into equation (19) yields, after some manipulation, u" at point 5

8

$$u_5'' = \frac{r_5\left[\left(v'' + \dfrac{F}{r}\right)_4 + \dfrac{\beta(ru'')_4}{r_\eta}\right] - F_2 - u_2'' \dfrac{\Delta\ell^2}{2\Delta x}}{\dfrac{\beta\, r_5^2}{r_\eta} + r_5\left(\dfrac{dh}{dx}\right)_5 + \dfrac{\Delta\ell^2}{2\Delta x}} \tag{26}$$

Equations (19) and (26) give the values of the angle-of-attack flow properties at body point 5. The solutions of all other body points are obtained in a manner similar to the one described above.

The Method of Obtaining Starting Values

It follows from the conditions for linearization of the potential equation that only pointed bodies of revolution can be treated by the procedure described in this analysis.

Beginning at the apex of the body of revolution, the initial Mach line or left-running characteristic line is constructed. The inclinations of the characteristic lines are given by the relations

$$\frac{\Delta r}{\Delta x} = \tan \mu = \frac{1}{\beta} \qquad \text{(left-running)}$$

and

$$\frac{\Delta r}{\Delta x} = \tan(-\mu) = -\frac{1}{\beta} \ . \qquad \text{(right-running)}$$

After choosing a suitable step size, the first point on the initial Mach line is located. In Figure 1, this is point 1. The right-running characteristic line is drawn from this point and intersects the body at point 2. The portion of the body between the apex and point 2 is replaced by a cone formed by the chord line between these two points. Therefore, the flow in the triangular region formed by the apex, point 1, and point 2 is conical, thus enabling us to begin the characteristics solution.

Because of assumed parallel flow at point 1, we have $u' = u'' = v' = 0$, $F = r$, and $v'' = 1$. Therefore, we also have $v'' + \dfrac{F}{r} = 2$. If we introduce the easily proved geometrical relation

$$r_\eta = \frac{h_0}{4}\left(3 + \frac{1}{\beta \tan \vartheta_0}\right)$$

into equation (18b), we obtain for axisymmetric flow

$$u_2' = - \frac{4 \tan^2 \vartheta_0}{1 + 3\beta \tan \vartheta_0 + 4 \tan^2 \vartheta_0} \quad . \tag{27}$$

Introducing the geometrical relation into equation (26) we obtain for flow due to angle of attack

$$u_2'' = \frac{(1 + 3\beta \tan \vartheta_0) \sin 2\vartheta_0}{(1 + 3\beta \tan \vartheta_0)(1 + \sin^2 \vartheta_0) + 4\beta^2 \sin^2 \vartheta_0} \quad , \tag{28}$$

where h_0 is the body radius at point 2 and ϑ_0 is the semi-apex angle. Equations (27) and (28) are independent of the body radius within their range of validity

$$\frac{dh}{dx} = \vartheta_0 = \text{CONSTANT}$$

and thus represent the approximate solution for conical flow.

Cone-Cylinder Bodies

In the solution of the flow field about cone-cylinder bodies by the methods described previously, we can see from the boundary conditions in equations (16) and (17) that a discontinuity in h, e. g. , at x = k in Figure 2, results in a discontinuity in the calculation of the flow properties at that point. Therefore, it is necessary to calculate the flow properties at the body both upstream and downstream of the point of discontinuity, although the physical coordinates of the point are the same in each case. Because of the necessity of this double calculation at this point, the reflected characteristic from there produces a discontinuity in the calculation of the flow properties at each field point along the "double" characteristic.

To explain the upstream and downstream calculation of the flow properties at the slope discontinuity on the body, we will consider points 5 and 6 of the configuration in Figure 2. The values of the flow properties upstream of the slope discontinuity are obtained by simply applying equations (16), (18b), (19), and (26) at point 5. The zero angle-of-attack flow properties downstream of the singular point are found by reapplying equations (16) and (18b) at point 6; however, in this case, $\frac{dh}{dx}$, which is double-valued at the corner, assumes its downstream value. The relations which give the values of the angle-of-attack flow properties

downstream of the singular point cannot be used as they appear in equations (19) and (26) due to the terms, $\frac{\Delta\ell^2}{2\Delta x}$ and F_5. It can be shown, however, that in the limit as $\Delta x \to 0$, $\frac{\Delta\ell^2}{2\Delta x} \to 0$ and that F does not change at the singular point; i.e., $F_5 = F_6$. Therefore, the relations which give the angle-of-attack flow properties at point 6 are with $r_5 = r_6 = r_\eta$

$$u''_6 = \frac{r_6\left(v'' + \frac{F}{r}\right)_5 + \beta(ru'')_5 - F_5}{\beta r_6 + r_6\left(\frac{dh}{dx}\right)_6} \tag{29}$$

and

$$v''_6 = u''_6 \left(\frac{dh}{dx}\right)_6 . \tag{30}$$

The calculation of the field points on the left-running "double" characteristic from the corner follows the usual procedure outlined earlier, i.e., the application of equations (11), (12), (13) and (14). The distinction of this calculation from any other lies only in the proper selection of base points on the left-running characteristic and in the case of the calculation of the downstream point (e.g., point 10 in Fig. 2) and in the interpretation of r_η. In this case r_η is simply $r_9 = r_{10}$ since the points 9 and 10 are physically coincident.

It is desirable in the cone-cylinder case to have several intermediate points on the right-running characteristic which intersects the expansion corner so that the flow field downstream of the corner will be as accurate as possible. For this reason we choose the initial step on the cone, i.e., the two point conical approximation as given by equations (27) and (28), to be a fraction of the total cone length.

Pressure Relations and Force Coefficients

According to Oswatitsch and Erdmann [4], the pressure coefficient at angle-of-attack α is given by the relation

$$C_p = -2(u' + u''\alpha\cos\psi) + \alpha^2\left(1 - \frac{F^2}{r^2}\sin^2\psi\right)$$

$$- v'^2 + \beta^2(u' + u''\alpha\cos\psi)^2 . \tag{31}$$

11

For small angles of attack, the second order terms in α may be neglected, and we obtain

$$C_p = C_{p_1} + C_{p_2} \, \alpha \cos \psi, \qquad (32)$$

where $C_{p_1} = \beta^2 \, u'^2 - 2u' - v'^2$ is the pressure coefficient at zero angle of attack and $C_{p_2} = 2u'' \, (\beta^2 \, u'' - 1)$.

The normal force coefficient is given by

$$C_N = -\frac{2}{S(L)} \int_o^L \int_o^\pi C_p \cos \psi \, h \, d\psi \, dx . \qquad (33)$$

Introducing equation (32) into equation (33) and differentiating with respect to α, we get the normal force coefficient slope

$$C_{N_\alpha} = \frac{d(C_N)}{d\alpha} = -\frac{\pi}{S(L)} \int_o^L C_{p_2} \cdot h \cdot dx . \qquad (34)$$

It follows immediately from equation (34) that the local normal force variation is given by

$$\frac{d(C_{N_\alpha})}{dx} = -\frac{\pi}{S(L)} \cdot C_{p_2} \cdot h .$$

RESULTS AND DISCUSSION

The Sauer-Heinz and Oswatitsch-Erdmann methods were programmed in Fortran IV to solve flow fields varying in body shape, body fineness ratio, and Mach number. To investigate the limits of applicability of these methods, the results of these computations were compared with J. L. Sims' exact method of characteristics* , the linear theory of Reference 1, and experimental data.

---

* Sims, J. L.: Results of Method of Characteristics Analysis at Small Angle of Attack (Unpublished). Aero-Dynamics Division of NASA, Marshall Space Flight Center, 1965

The approach taken by Sims is based upon a small angle-of-attack perturbation superimposed on a nonlinear axisymmetric flow field which is determined by the method of characteristics (eqs. 26-15, 26-16, 26-17, and 26-18 in Ref. 5).

For comparison of the zero angle-of-attack flow properties computed by the Sauer-Heinz method, the pressure coefficient was computed for convex and concave parabolic ogives. The equations of these ogives are

$$h(x) = \frac{\epsilon}{2} (x + x^2) \qquad \text{concave ogive}$$

and

$$h(x) = \epsilon (2x - x^2) . \qquad \text{concave ogive}$$

The values of the body fineness ratio, ϵ, used in these computations were 0.05, 0.10, 0.15, and 0.20, and the Mach numbers were 1.5 and 3.0. These results are given in Figures 3 through 18. The pressure coefficients were also computed for 5-degree and 10-degree cone-cylinder bodies at Mach numbers of 1.5 and 3.0 and an ogival body whose configuration is given by the equation $h(x) = \frac{1}{3} x - \frac{10}{36} x^2$ [1] at Mach numbers of 1.84, 2.45, and 3.01. These results are given in Figures 19 through 25.

For comparison of the angle-of-attack flow properties computed by the Oswatitsch-Erdmann method, the normal force coefficient slope was computed and plotted as a function of Mach number for the convex and concave ogives and the 5-degree and 10-degree cone-cylinders. These results appear in Figures 26 through 31. Also, the local normal force variation was computed for the convex and concave ogives at Mach numbers of 1.5 and 3.0 and the ogival body [1] at Mach numbers of 1.84, 2.45 and 3.01. These results appear in Figures 32 through 42.

For comparison of the Oswatitsch-Erdmann method with experimental data, the local normal force variation was computed for a convex parabolic ogive with body fineness ratios of 0.066, 0.1, and 0.1667 at Mach numbers of 1.59, 3.0, and 4.25 and also for a 10-degree cone-cylinder at Mach numbers of 1.99 and 2.44. These results appear in Figures 43 through 49.

Figures 3 through 18 show that the Sauer-Heinz method agrees closely with Sims' method for body fineness ratios of 0.15 or less; however, for a body fineness ratio of 0.20 they begin to deviate considerably, especially at the higher Mach number. These two methods compare very well for the 5-degree and 10-degree cone-cylinders also. In view of the assumptions made in the

13

linearization of the potential equation, this is exactly the trend that one would expect. This same trend can be observed when comparing the Oswatitsch-Erdmann method with Sims' method in Figures 26 through 39. Although the range of values for the body fineness ratios and Mach numbers in the experimental data is somewhat limited, the trend seems to be present there also. Figures 19 through 21 and 40 through 42 show that the comparison between these methods and the linear theory of Reference 1 is very good except at the apex of the body. This disagreement there could be attributed to the size of the initial step-length used in the conical approximation flow region, from which the starting values are obtained.

CONCLUDING REMARKS

The truncation error in the numerical solution was studied by systematically varying the field mesh width. A constant step-length in the entire field was used. Step-lengths in the range 0.0025 → 0.0200 were tried to increments of 0.0025. The truncation error was found to be sufficiently small with a step-length of 0.01, which was then used to compute all of the solutions for this report. Using this step-length, the average time for a complete run for both zero and nonzero angle-of-attack solutions at one Mach number was about thirteen seconds on the IBM 7094 digital computer.

A careful study of the comparisons of the Sauer-Heinz and Oswatitsch-Erdmann linear methods given in the figures shows that these methods are applicable to flow fields where the hypersonic similarity parameter, $M_\infty \epsilon$, is less than about 0.6

George C. Marshall Space Flight Center
National Aeronautics and Space Administration
Huntsville, Alabama, April 19, 1966
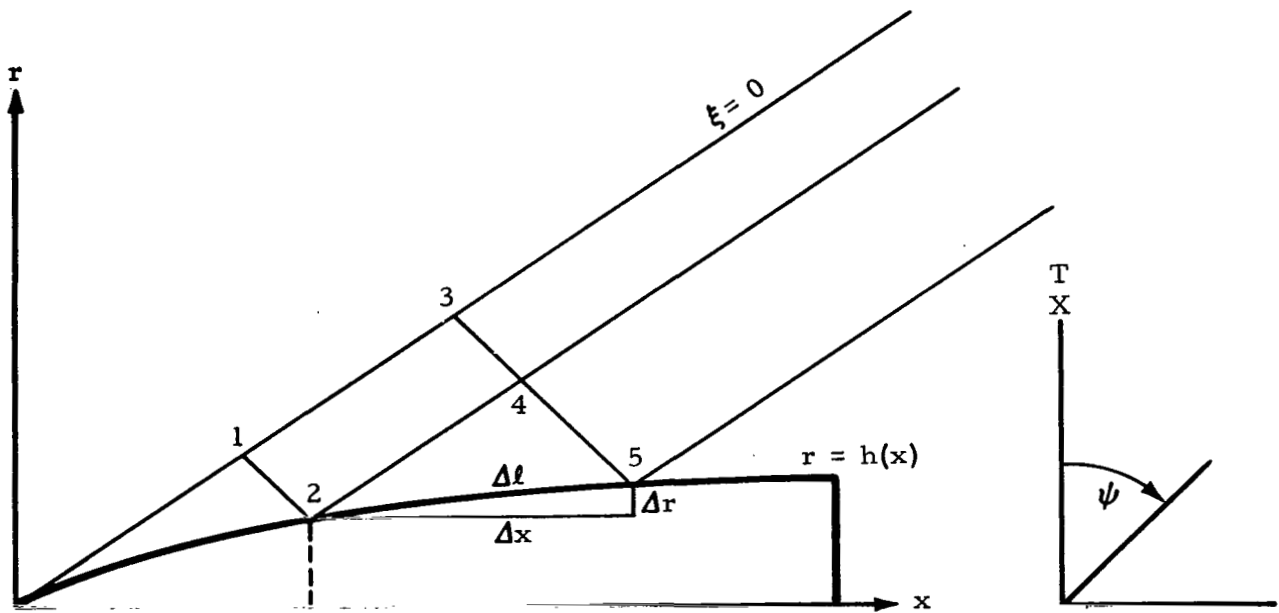
FIGURE 1.   ILLUSTRATION OF SMOOTH BODY CALCULATION
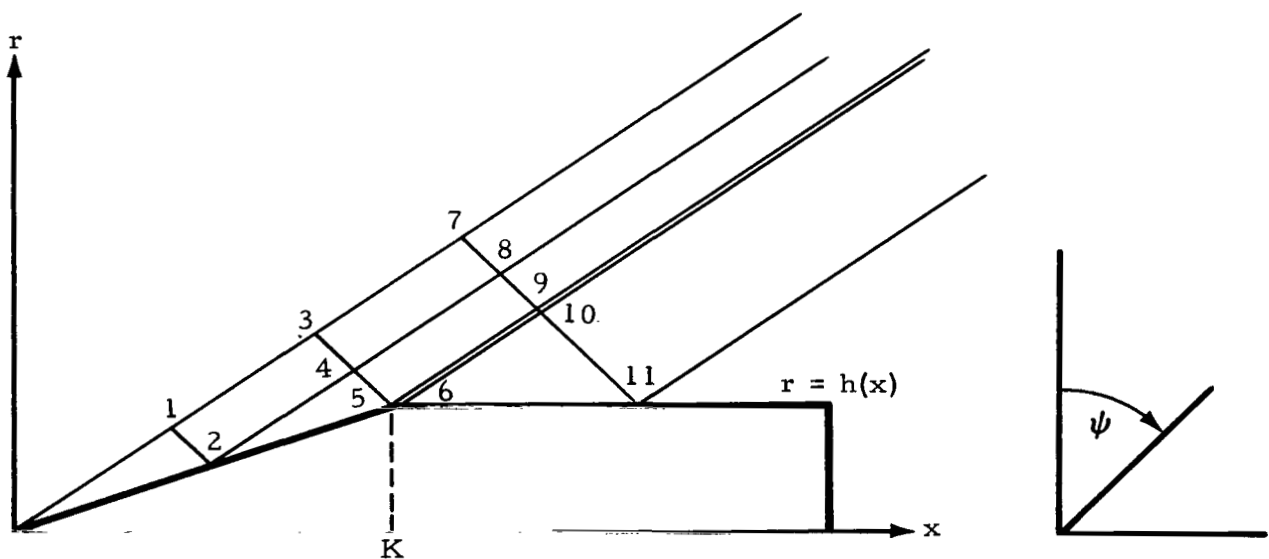
FIGURE 2.   ILLUSTRATION OF CONE-CYLINDER BODY CALCULATION
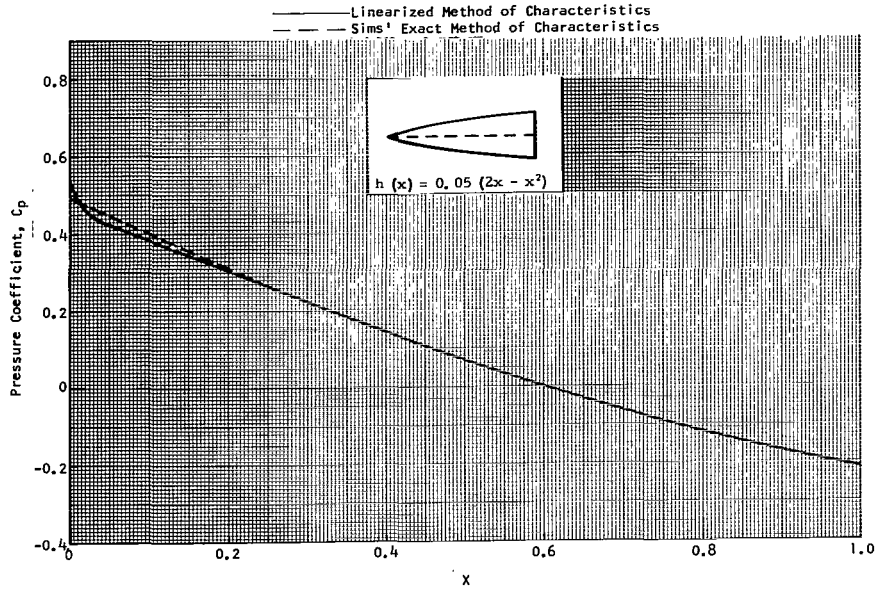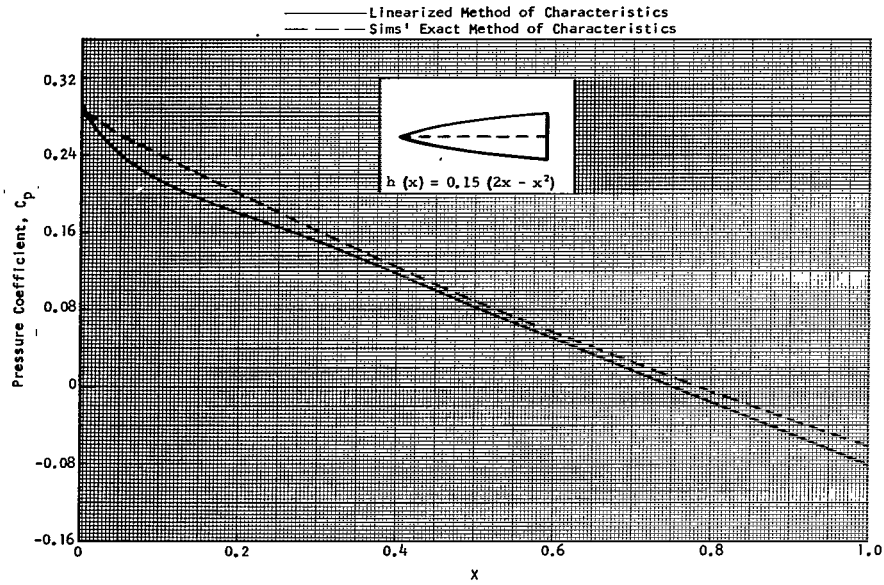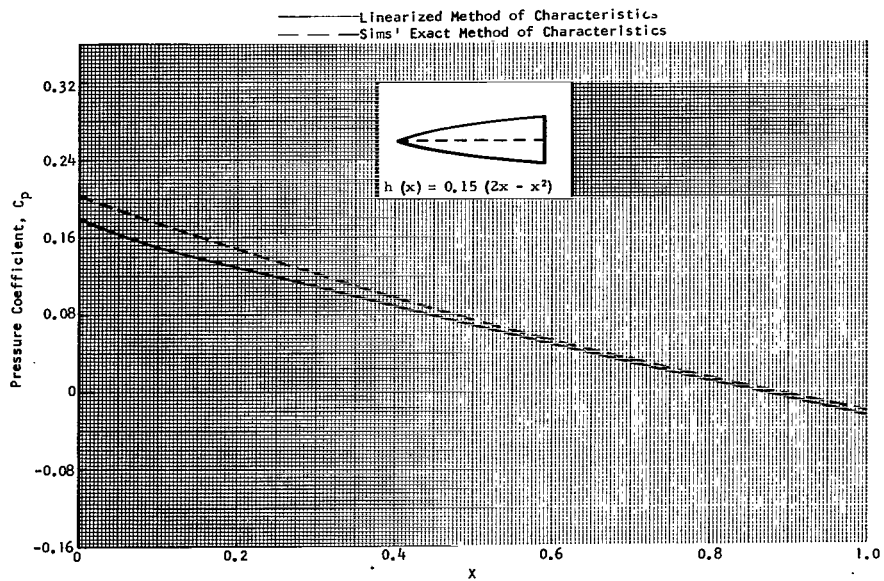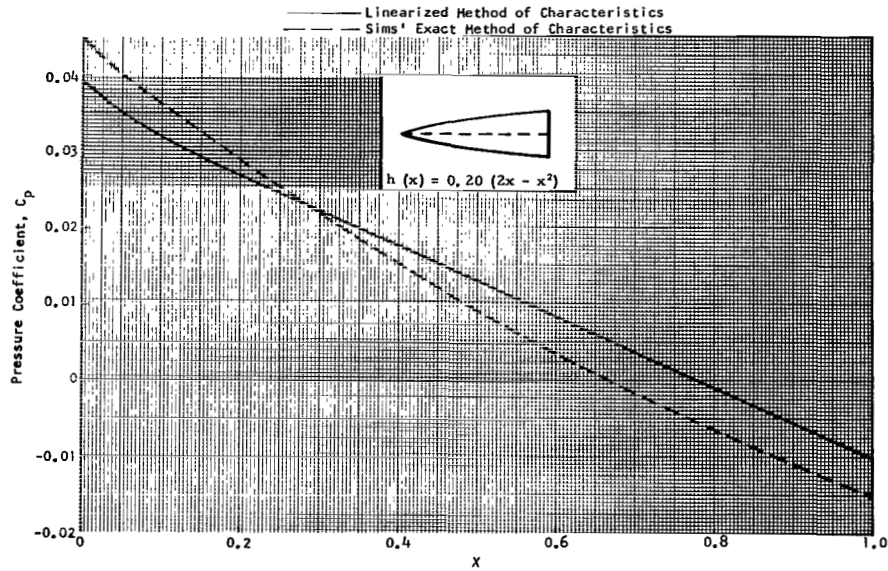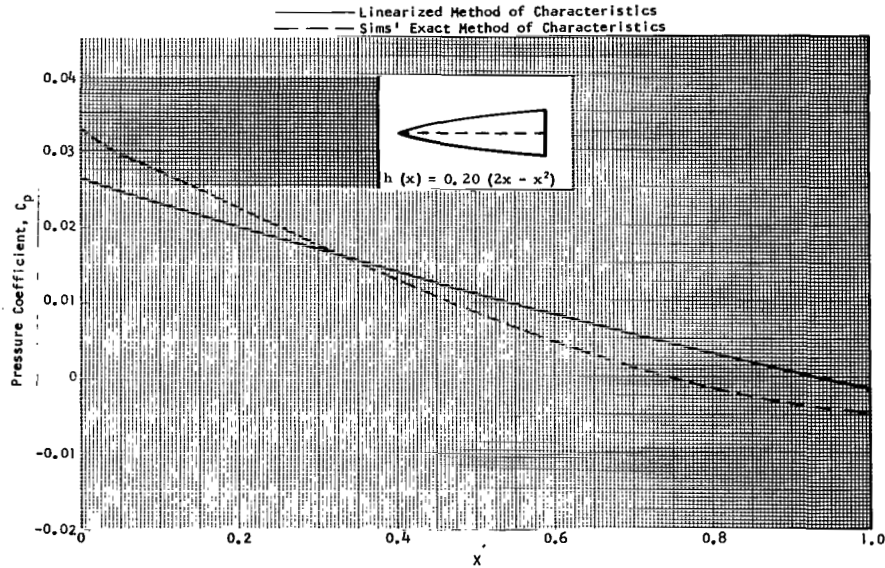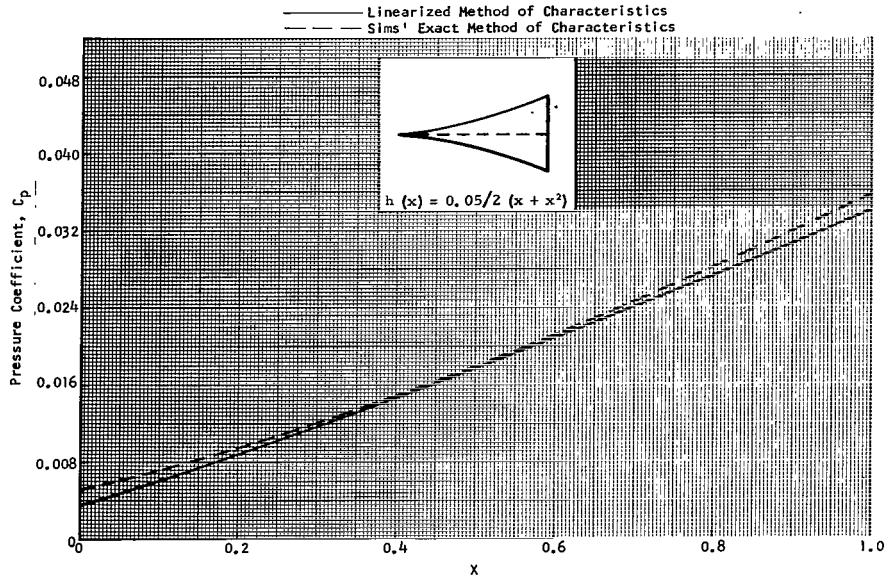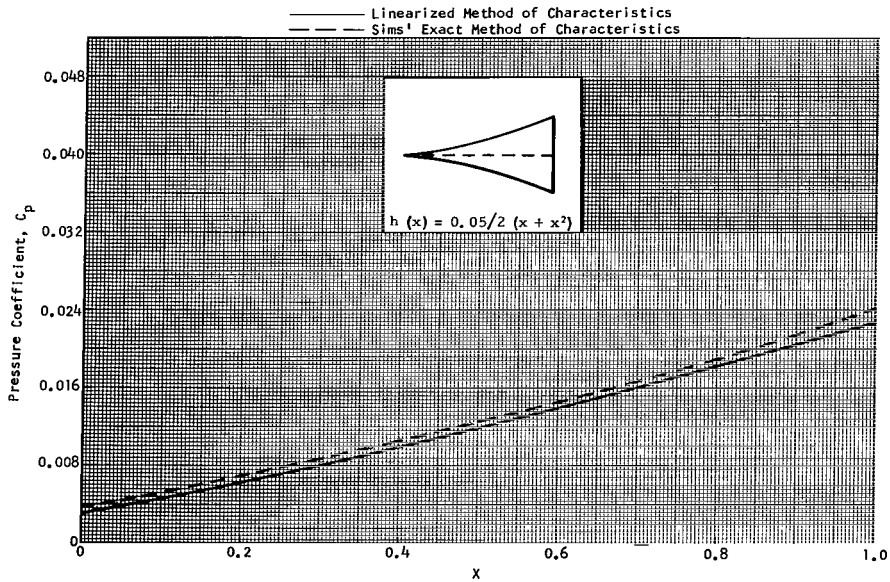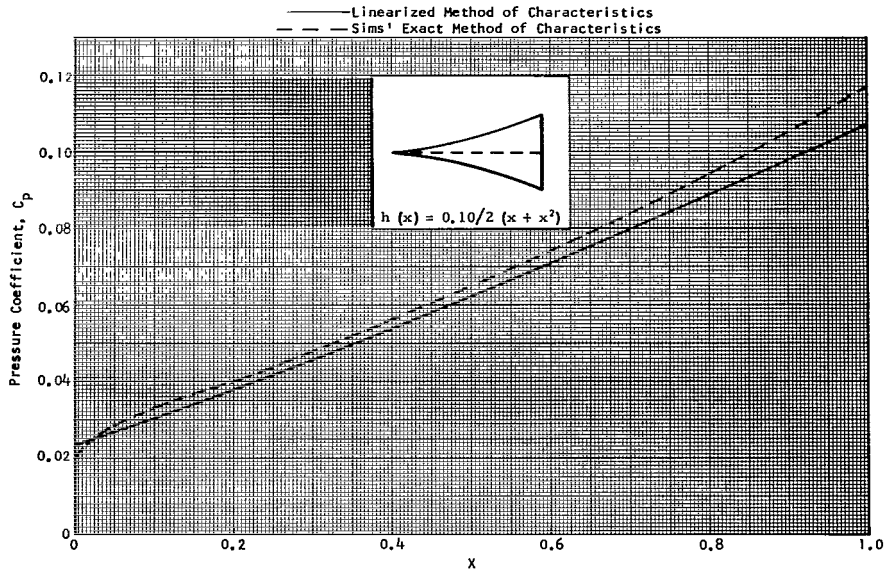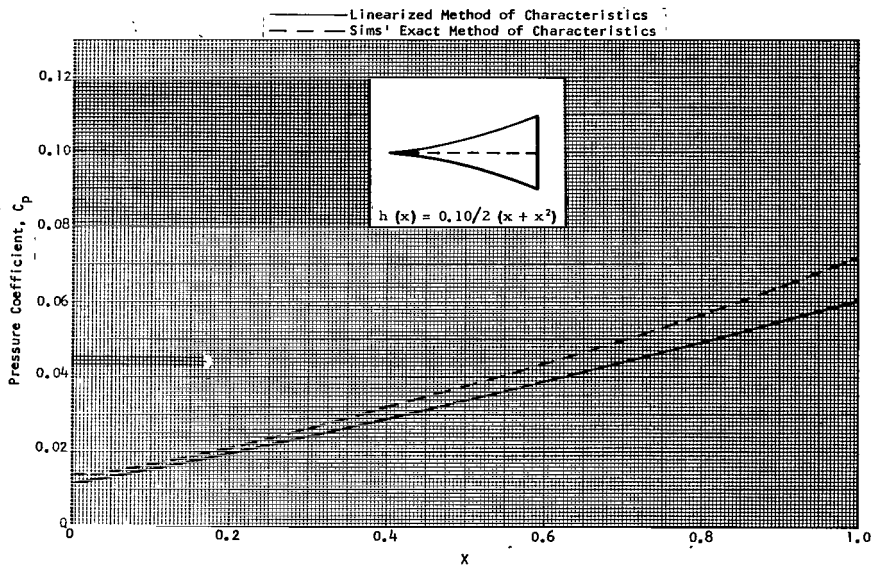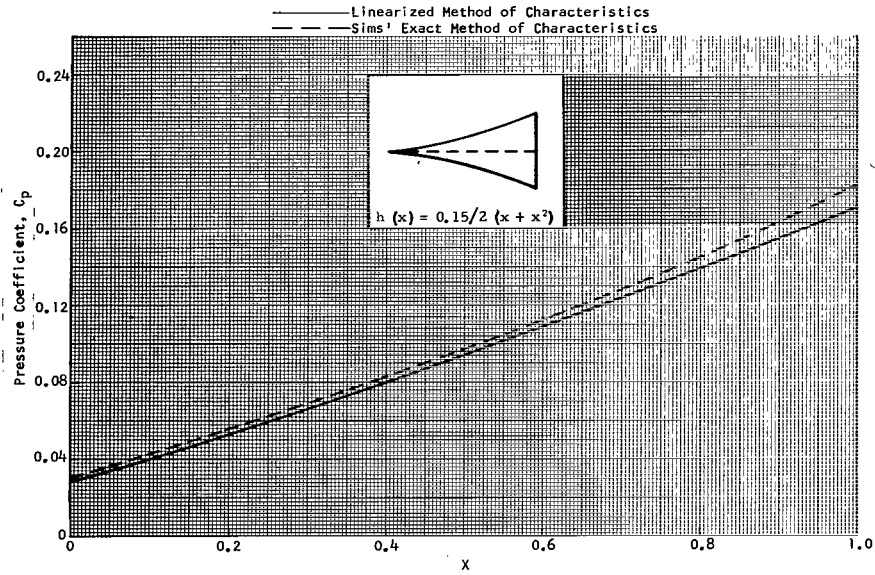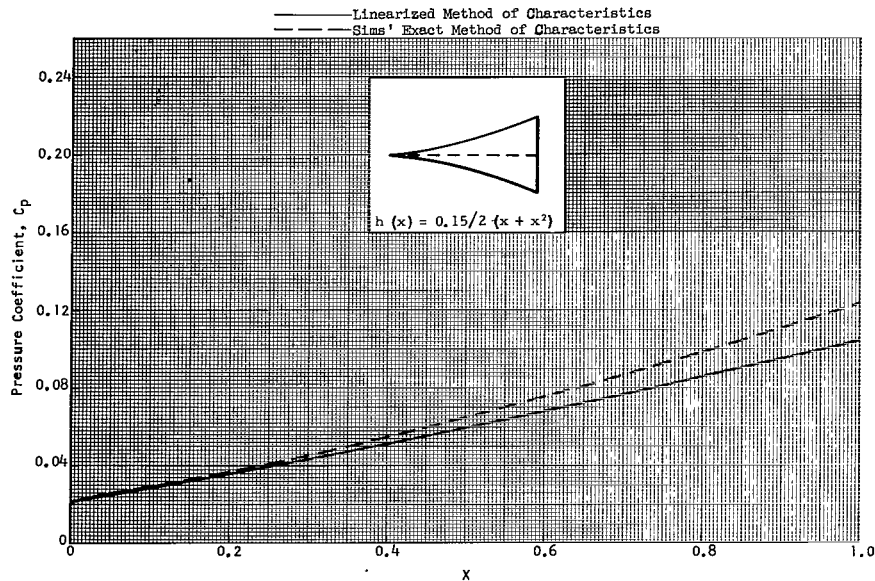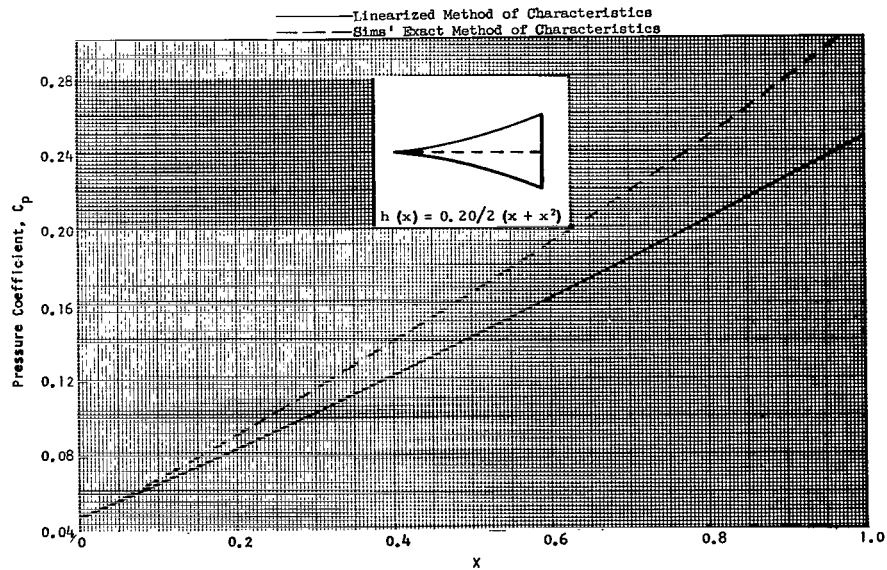
FIGURE 3.   PRESSURE DISTRIBUTION ALONG A CONVEX PARABOLIC OGIVE WITH
BODY FINENESS RATIO OF 0. 05 AT M_∞ = 1. 5
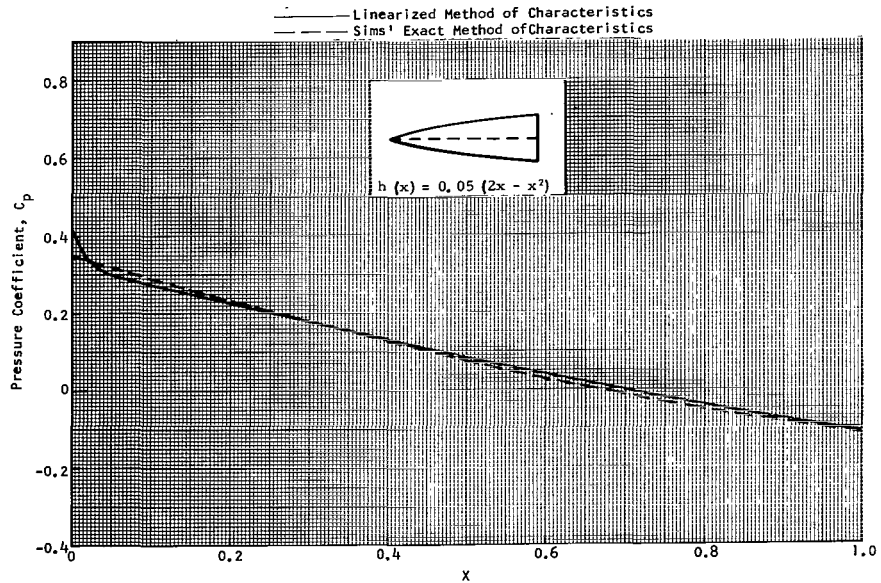
FIGURE 4.   PRESSURE DISTRIBUTION ALONG A CONVEX PARABOLIC OGIVE WITH
BODY FINENESS RATIO OF 0. 05 AT M_∞ = 3. 0

16

Pressure Coefficient, c_p

0.16

0.12

0.08

0.04

0

-0.04

-0.08

h (x) = 0.10 (2x - x²)

0   0.2   0.4   0.6   . 0.8   1.0

X
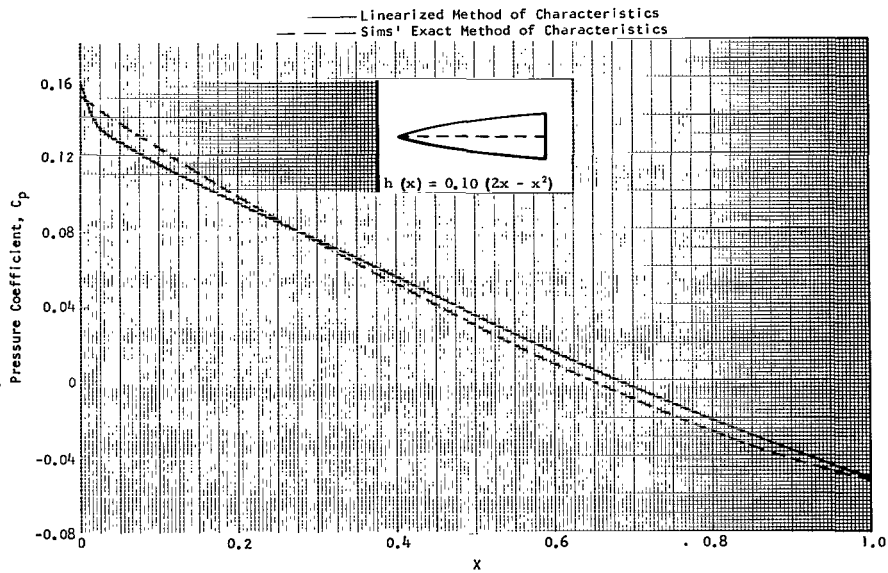
FIGURE 5.   PRESSURE DISTRIBUTION ALONG A CONVEX PARABOLIC OGIVE WITH BODY FINENESS RATIO OF 0.10 AT M_∞ = 1.5

Linearized Method of Characteristics
Sims' Exact Method of Characteristics

Pressure Coefficient, c_p

0.16

0.12

0.08

0.04

0

-0.04

-0.08

h (x) = 0.10 (2x - x²)

0   0.2   0.4   0.6   .0.8   1.0
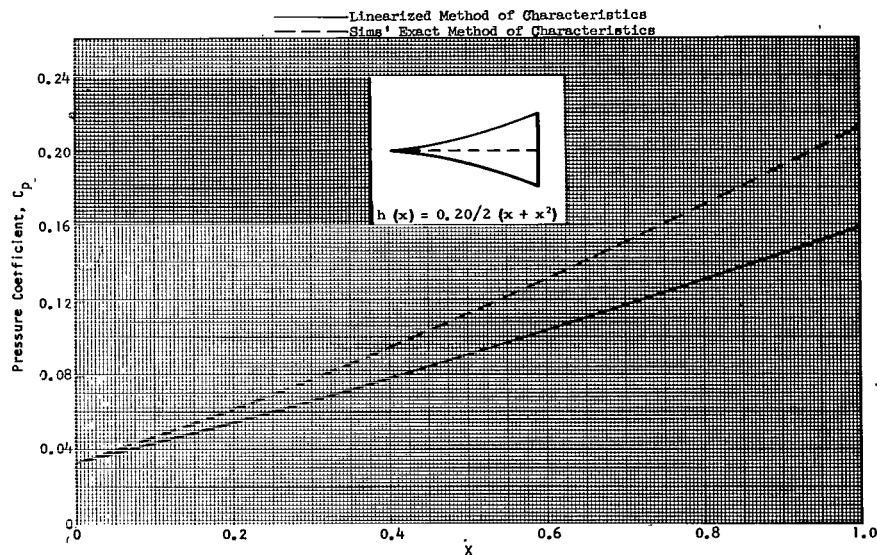
X
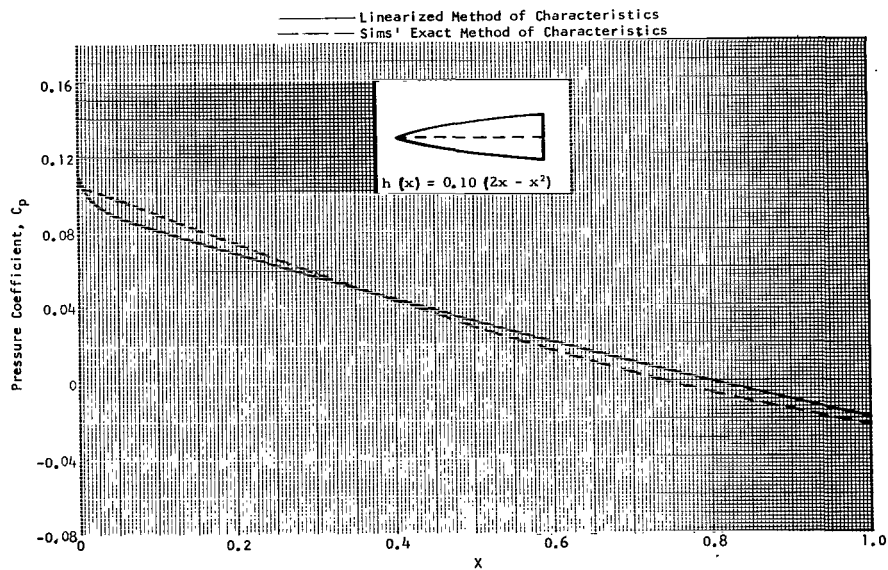
FIGURE 6.   PRESSURE DISTRIBUTION ALONG A CONVEX PARABOLIC OGIVE WITH BODY FINENESS RATIO OF 0.10 AT M_∞ = 3.0

17

FIGURE 7. PRESSURE DISTRIBUTION ALONG A CONVEX PARABOLIC OGIVE WITH
BODY FINENESS RATIO OF 0.15 AT M_∞ = 1.5

FIGURE 8. PRESSURE DISTRIBUTION ALONG A CONVEX PARABOLIC OGIVE WITH
BODY FINENESS RATIO OF 0.15 AT M_∞ = 3.0

18

FIGURE 9. PRESSURE DISTRIBUTION ALONG A CONVEX PARABOLIC OGIVE WITH BODY FINENESS RATIO OF 0.20 AT $M_\infty = 1.5$

FIGURE 10. PRESSURE DISTRIBUTION ALONG A CONVEX PARABOLIC OGIVE WITH BODY FINENESS RATIO OF 0.20 AT $M_\infty = 3.0$

19

FIGURE 11.   PRESSURE DISTRIBUTION ALONG A CONCAVE PARABOLIC OGIVE WITH
BODY FINENESS RATIO OF 0.05 AT M_∞ = 1.5

FIGURE 12.   PRESSURE DISTRIBUTION ALONG A CONCAVE PARABOLIC OGIVE WITH
BODY FINENESS RATIO OF 0.05 AT M_∞ = 3.0

FIGURE 13.   PRESSURE DISTRIBUTION ALONG A CONCAVE PARABOLIC OGIVE WITH
BODY FINENESS RATIO OF 0. 10 AT M_∞ = 1. 5

FIGURE 14.   PRESSURE DISTRIBUTION ALONG A CONCAVE PARABOLIC OGIVE WITH
BODY FINENESS RATIO OF 0. 10 AT M_∞ = 3. 0

FIGURE 15. PRESSURE DISTRIBUTION ALONG A CONCAVE PARABOLIC OGIVE WITH BODY FINENESS RATIO OF 0. 15 AT M_∞ = 1. 5

FIGURE 16. PRESSURE DISTRIBUTION ALONG A CONCAVE PARABOLIC OGIVE WITH BODY FINENESS RATIO OF 0. 15 AT M_∞ = 3. 0

22

FIGURE 17. PRESSURE DISTRIBUTION ALONG A CONCAVE PARABOLIC OGIVE WITH
BODY FINENESS RATIO OF 0.20 AT $M_\infty = 1.5$

FIGURE 18. PRESSURE DISTRIBUTION ALONG A CONCAVE PARABOLIC OGIVE WITH
BODY FINENESS RATIO OF 0.20 AT $M_\infty = 3.0$

23
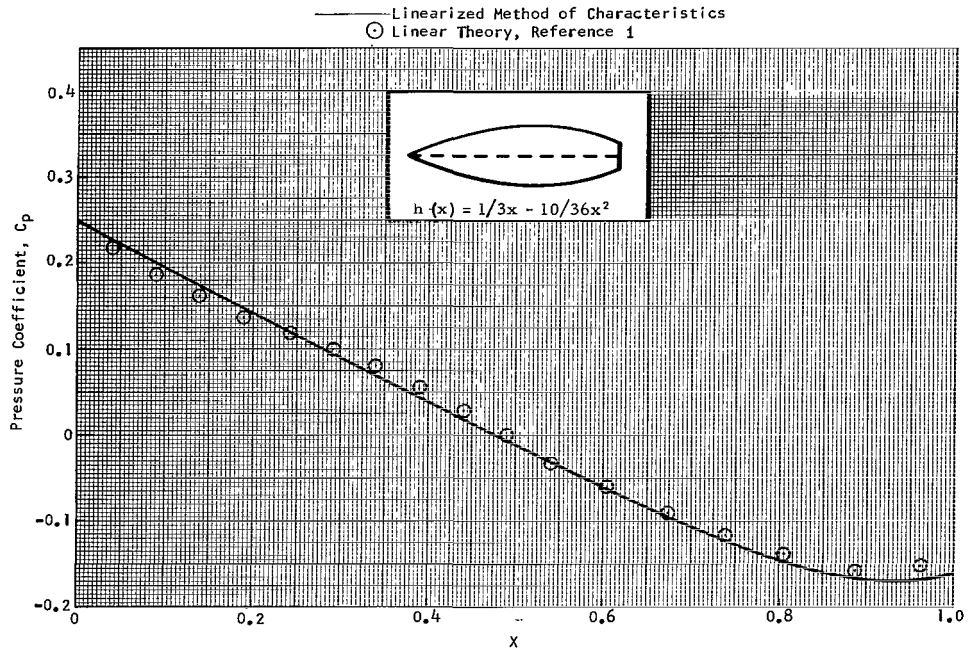
FIGURE 19.   PRESSURE DISTRIBUTION ALONG A BODY CONFIGURATION DESCRIBED
BY THE EQUATION, $h(x) = x/3 - 10x^2/36$, $M_\infty = 1.84$
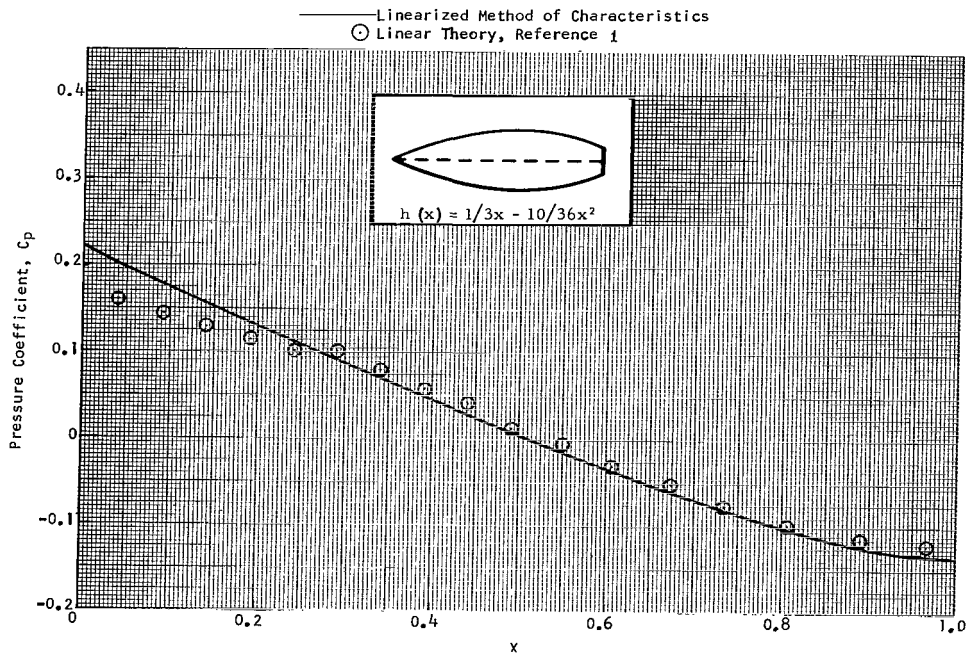
FIGURE 20.   PRESSURE DISTRIBUTION ALONG A BODY CONFIGURATION DESCRIBED
BY THE EQUATION, $h(x) = x/3 - 10x^2/36$, $M_\infty = 2.45$

$$h(x) = 1/3x - 10/36x^2$$
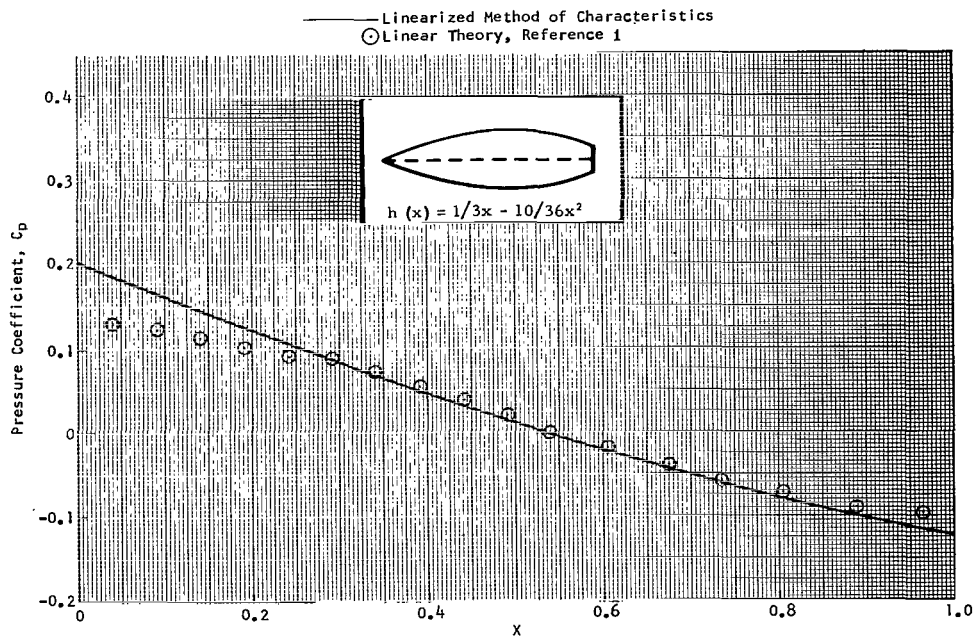
FIGURE 21.   PRESSURE DISTRIBUTION ALONG A BODY CONFIGURATION DESCRIBED BY THE EQUATION, $h(x) = x/3 - 10x^2/36$, $M_\infty = 3.01$
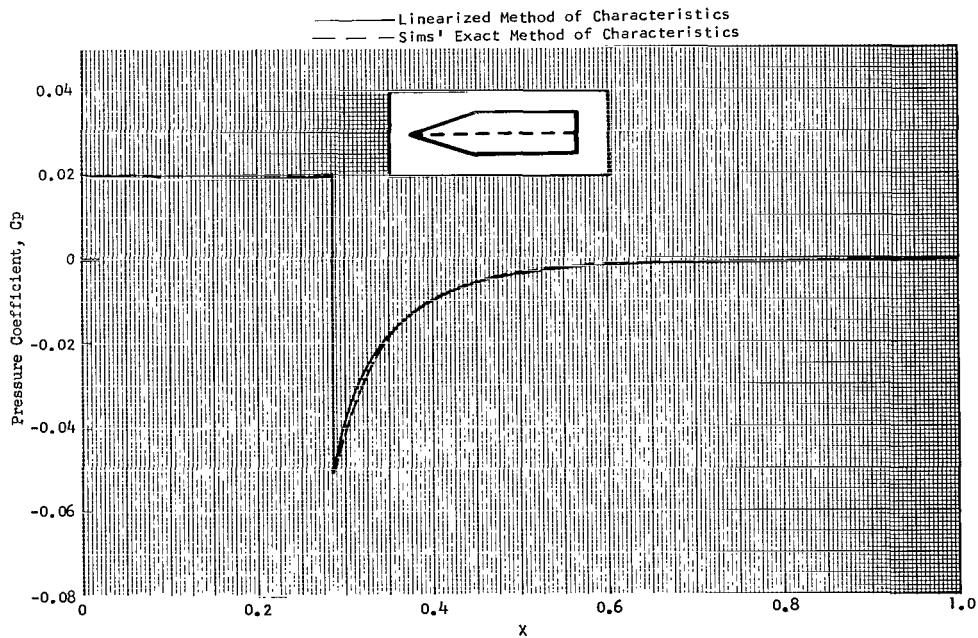
FIGURE 22.   PRESSURE DISTRIBUTION ALONG A 5 DEGREE CONE PLUS CYLINDER BODY, $M_\infty = 1.5$, $\epsilon = .05$
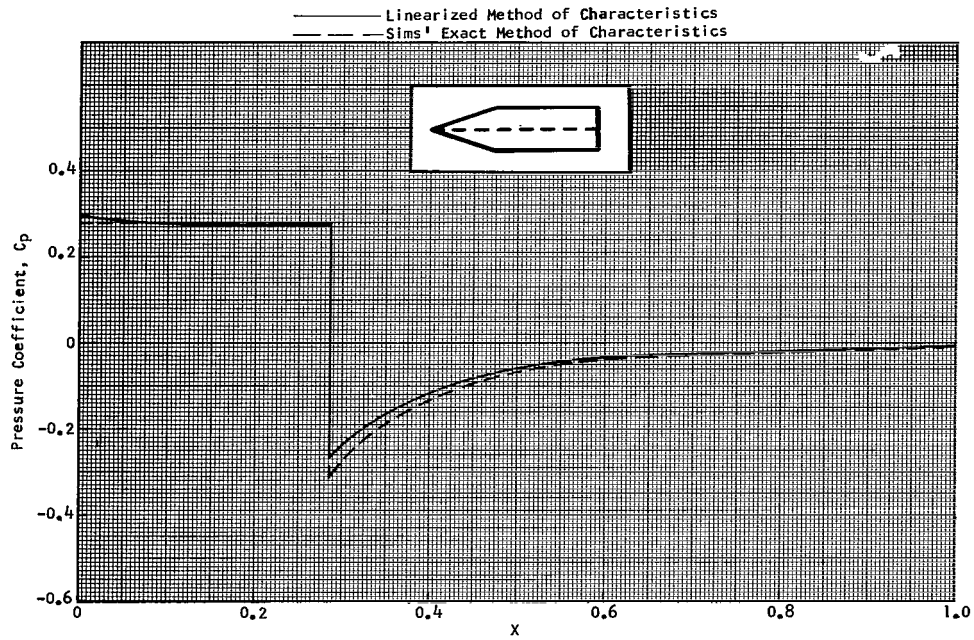
FIGURE 23. PRESSURE DISTRIBUTION ALONG A 5 DEGREE CONE PLUS CYLINDER BODY, $M_\infty = 3.0$, $\epsilon = .05$
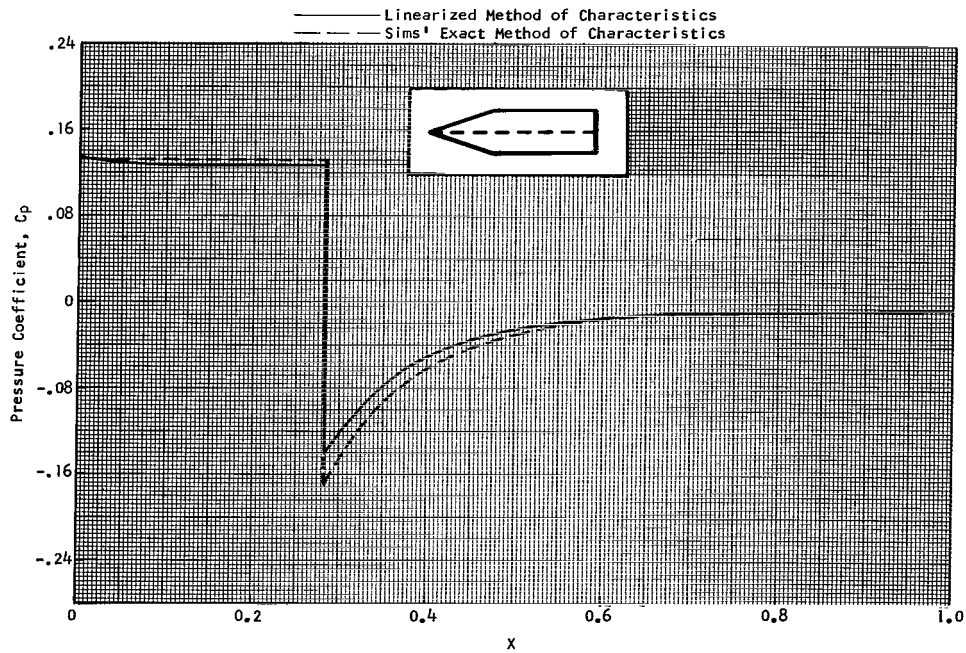
FIGURE 24. PRESSURE DISTRIBUTION ALONG A 10 DEGREE CONE PLUS CYLINDER BODY, $M_\infty = 1.5$, $\epsilon = .10$
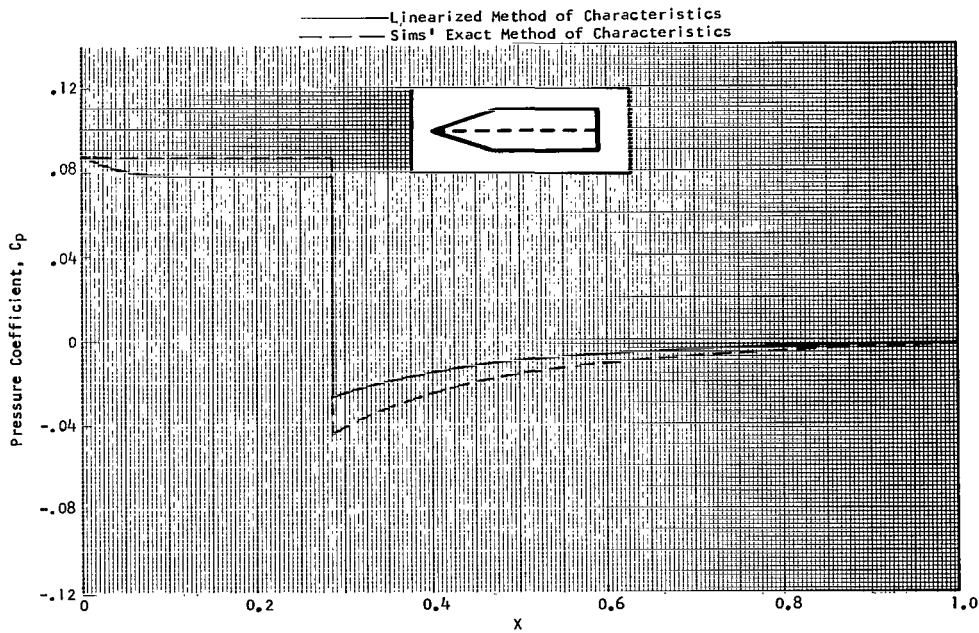
FIGURE 25. PRESSURE DISTRIBUTION ALONG A 10 DEGREE CONE PLUS CYLINDER BODY, $M_\infty = 3.0$, $\epsilon = .10$
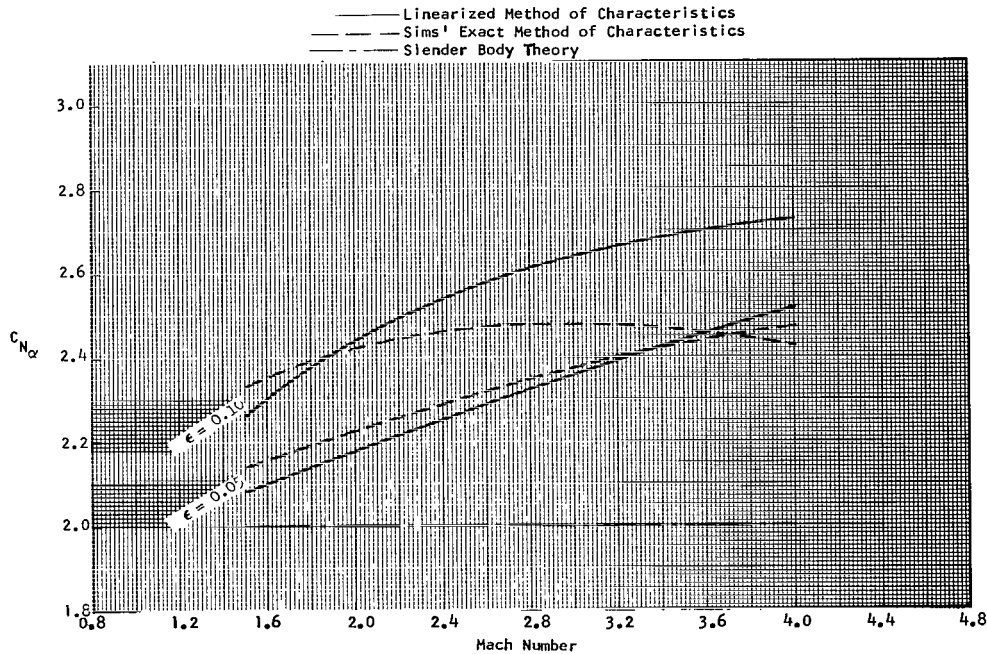
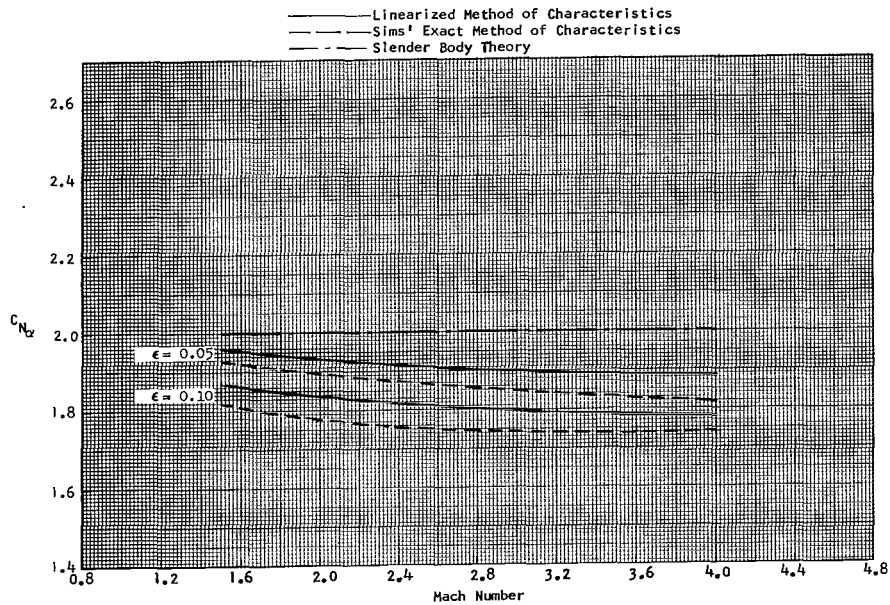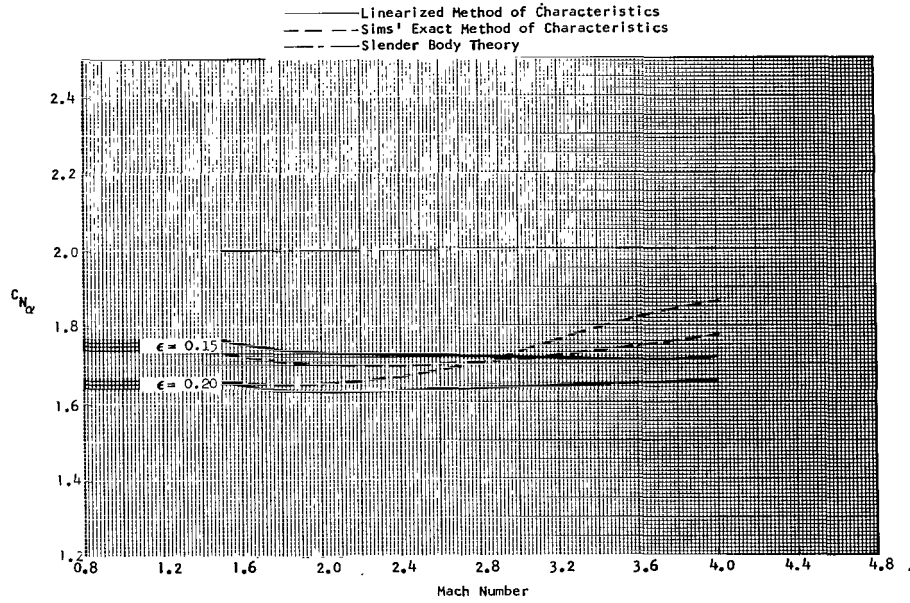FIGURE 26. EFFECT OF MACH NUMBER AND THICKNESS RATIO ON NORMAL FORCE COEFFICIENT SLOPE FOR A CONVEX PARABOLIC OGIVE

27
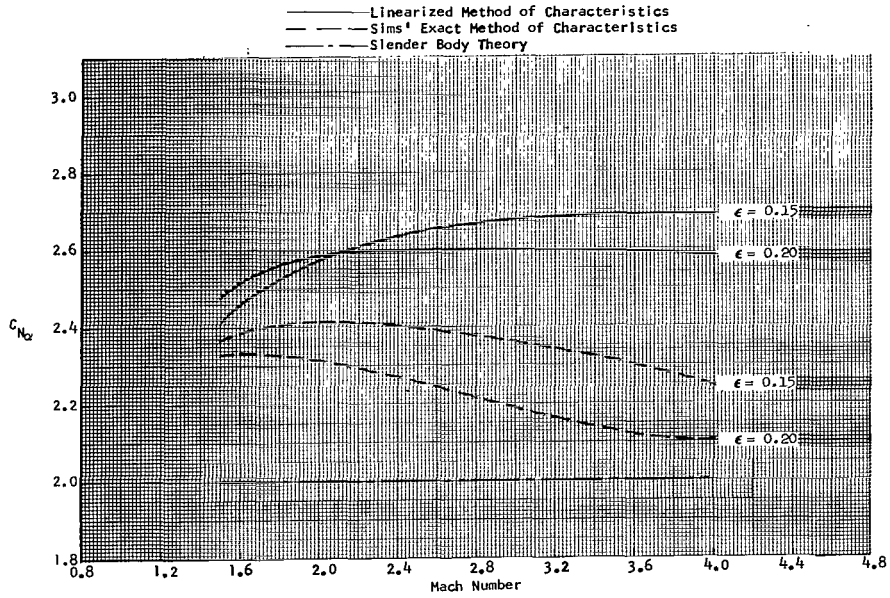
FIGURE 27. EFFECT OF MACH NUMBER AND THICKNESS RATIO ON NORMAL
FORCE COEFFICIENT SLOPE FOR A CONVEX PARABOLIC OGIVE

FIGURE 28. EFFECT OF MACH NUMBER AND THICKNESS RATIO ON NORMAL
FORCE COEFFICIENT SLOPE FOR A CONCAVE PARABOLIC OGIVE

C_{N_α}

$\epsilon = 0.15$

$\epsilon = 0.20$

Mach Number

FIGURE 29. EFFECT OF MACH NUMBER AND THICKNESS RATIO ON NORMAL
FORCE COEFFICIENT SLOPE FOR A CONCAVE PARABOLIC OGIVE

Linearized Method of Characteristics
Sims' Exact Method of Characteristics

C_{N_α}
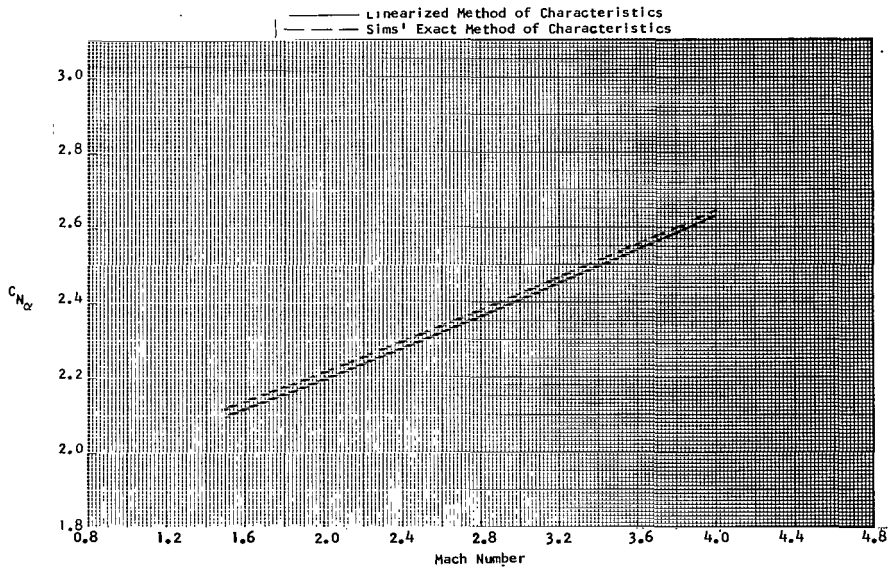
Mach Number

FIGURE 30. EFFECT OF MACH NUMBER ON THE NORMAL FORCE COEFFICIENT
SLOPE FOR A 5 DEGREE CONE PLUS CYLINDER BODY
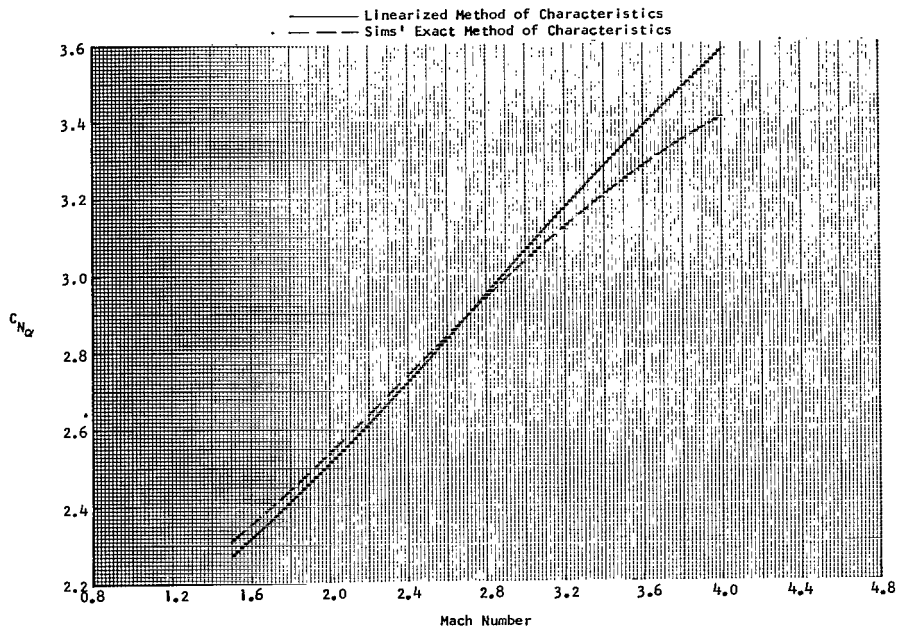
FIGURE 31.   EFFECT OF MACH NUMBER ON THE NORMAL FORCE COEFFICIENT
SLOPE FOR A 10 DEGREE CONE PLUS CYLINDER BODY
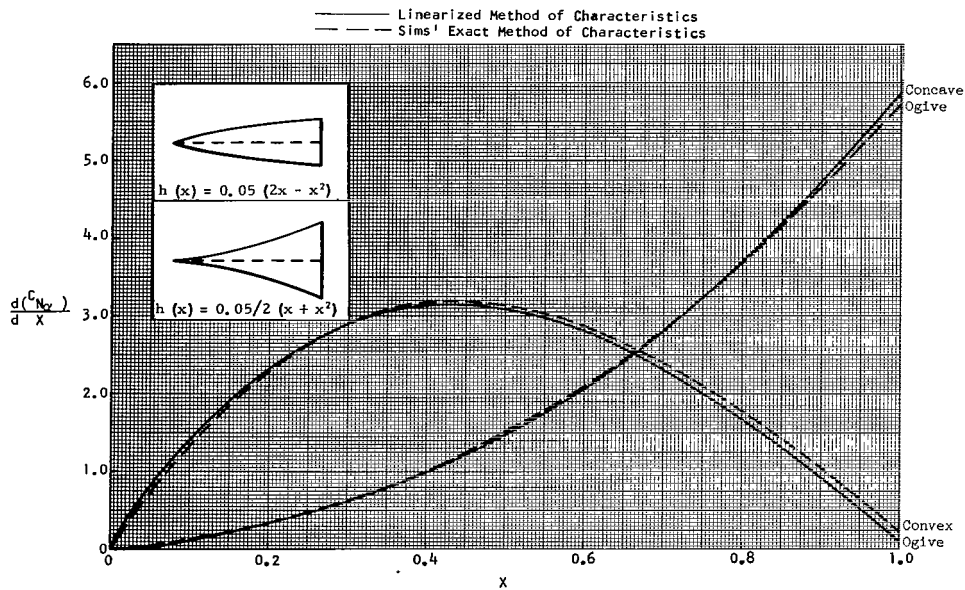
FIGURE 32.   LOCAL NORMAL FORCE VARIATION FOR CONVEX AND CONCAVE
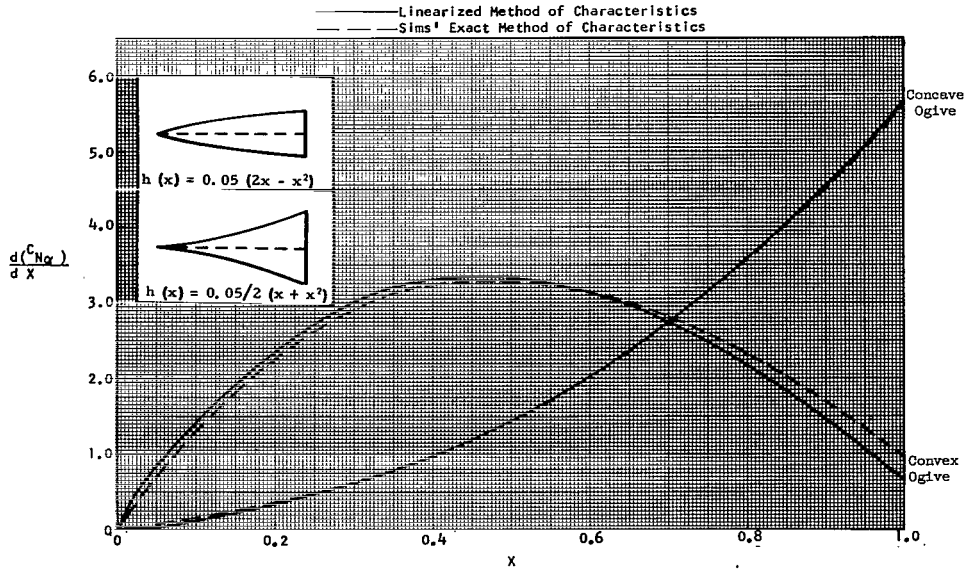OGIVES OF FINENESS RATIO 0.05 AT A MACH NUMBER OF 1.5

30

FIGURE 33. LOCAL NORMAL FORCE VARIATION FOR CONVEX AND CONCAVE
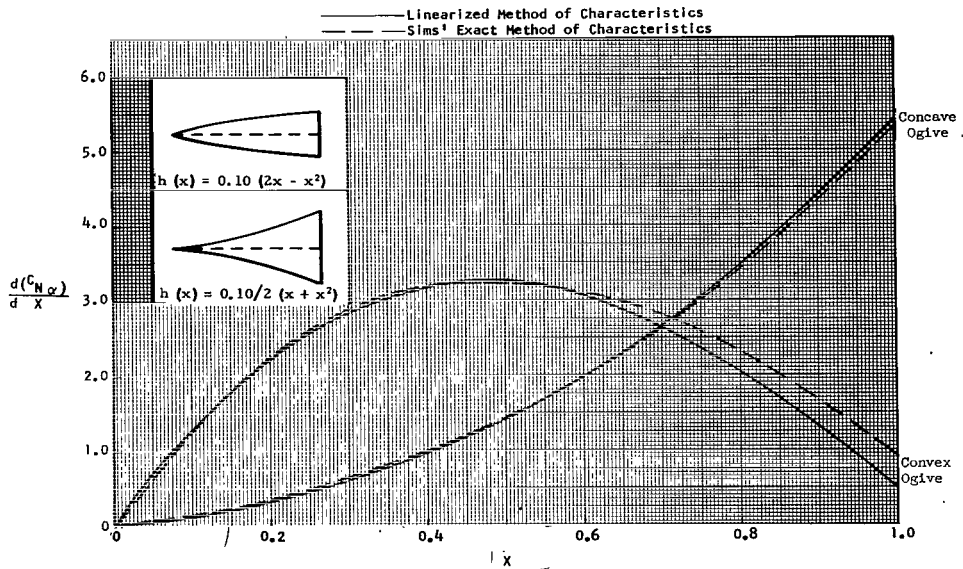OGIVES OF FINENESS RATIO 0. 05 AT A MACH NUMBER OF 3. 0

FIGURE 34. LOCAL NORMAL FORCE VARIATION FOR CONVEX AND CONCAVE
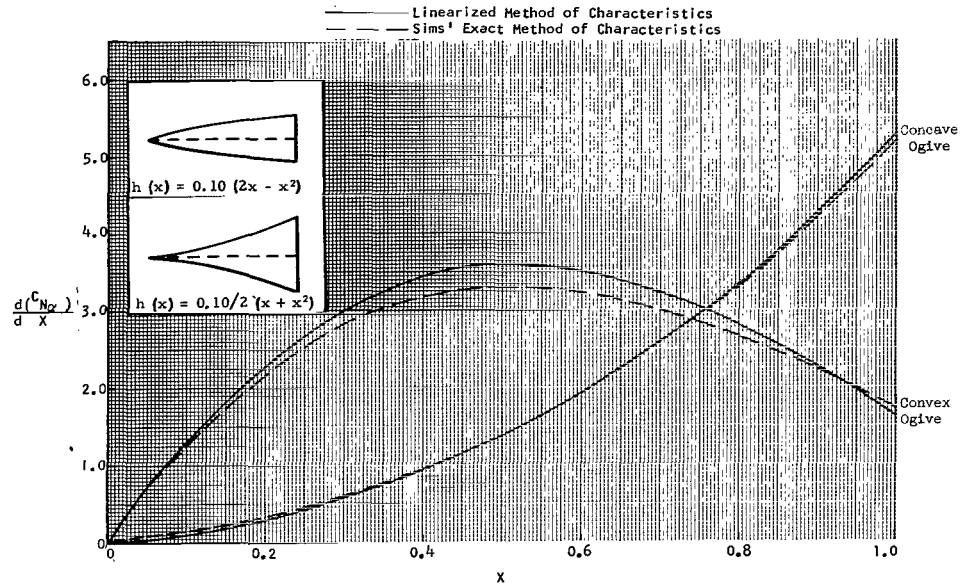OGIVES OF FINENESS RATIO 0. 10 AT A MACH NUMBER OF 1. 5

31

FIGURE 35.   LOCAL NORMAL FORCE VARIATION FOR CONVEX AND CONCAVE
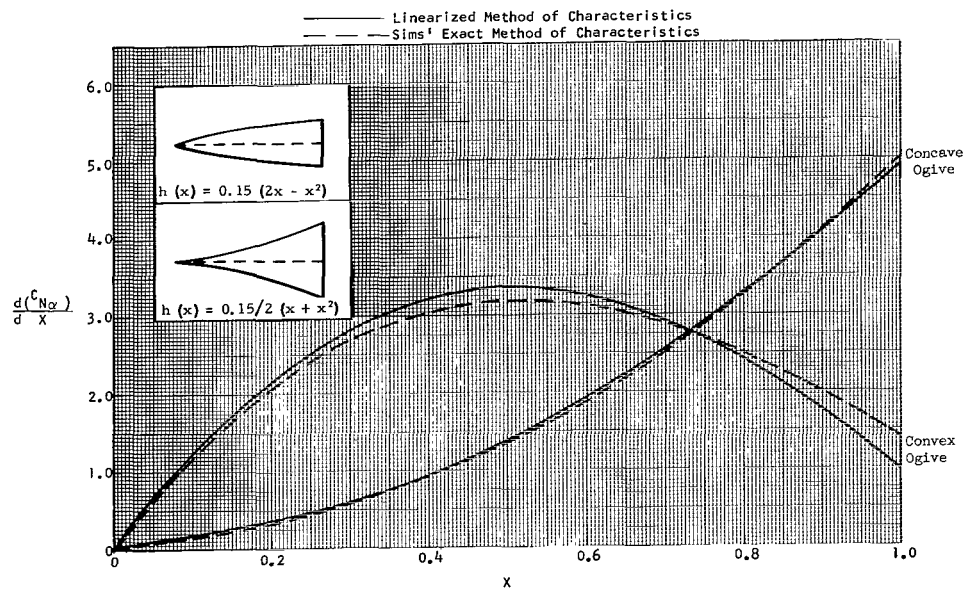OGIVES OF FINENESS RATIO 0.10 AT A MACH NUMBER OF 3.0

FIGURE 36.   LOCAL NORMAL FORCE VARIATION FOR CONVEX AND CONCAVE
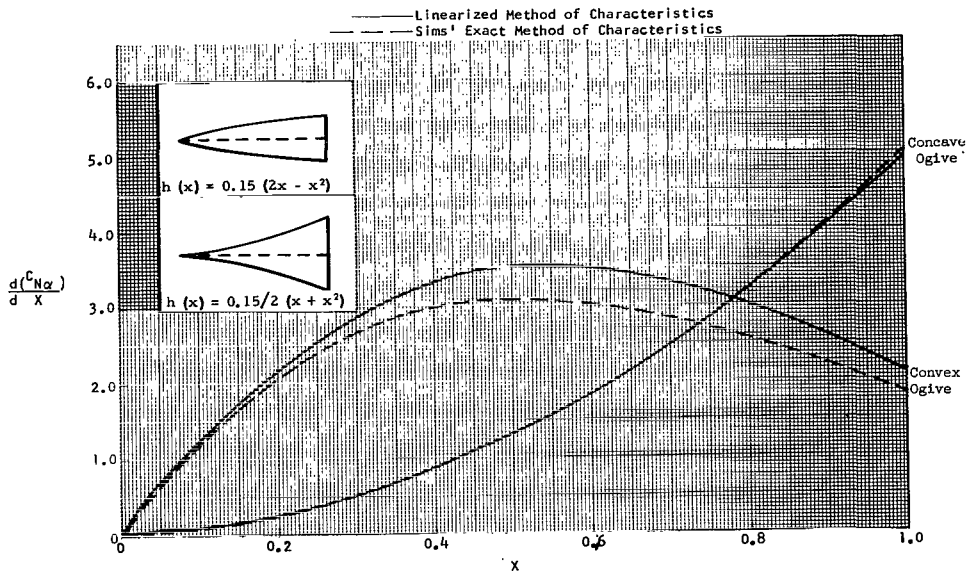OGIVES OF FINENESS RATIO 0.15 AT A MACH NUMBER OF 1.5

FIGURE 37. LOCAL NORMAL FORCE VARIATION FOR CONVEX AND CONCAVE OGIVES OF FINENESS RATIO 0.15 AT A MACH NUMBER OF 3.0
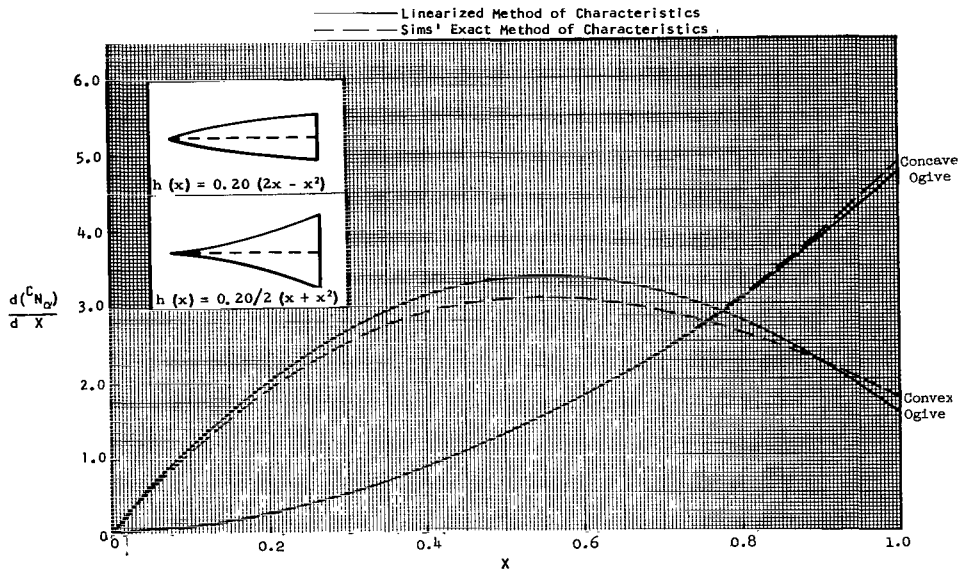

FIGURE 38. LOCAL NORMAL FORCE VARIATION FOR CONVEX AND CONCAVE OGIVES OF FINENESS RATIO 0.20 AT A MACH NUMBER OF 1.5
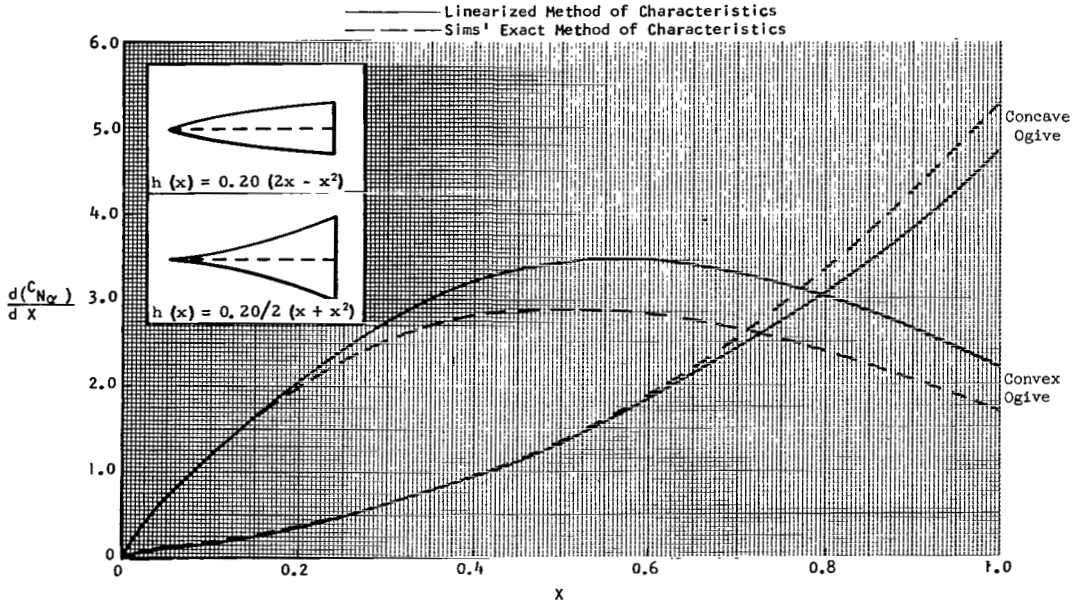
33

FIGURE 39.   LOCAL NORMAL FORCE VARIATION FOR CONVEX AND CONCAVE
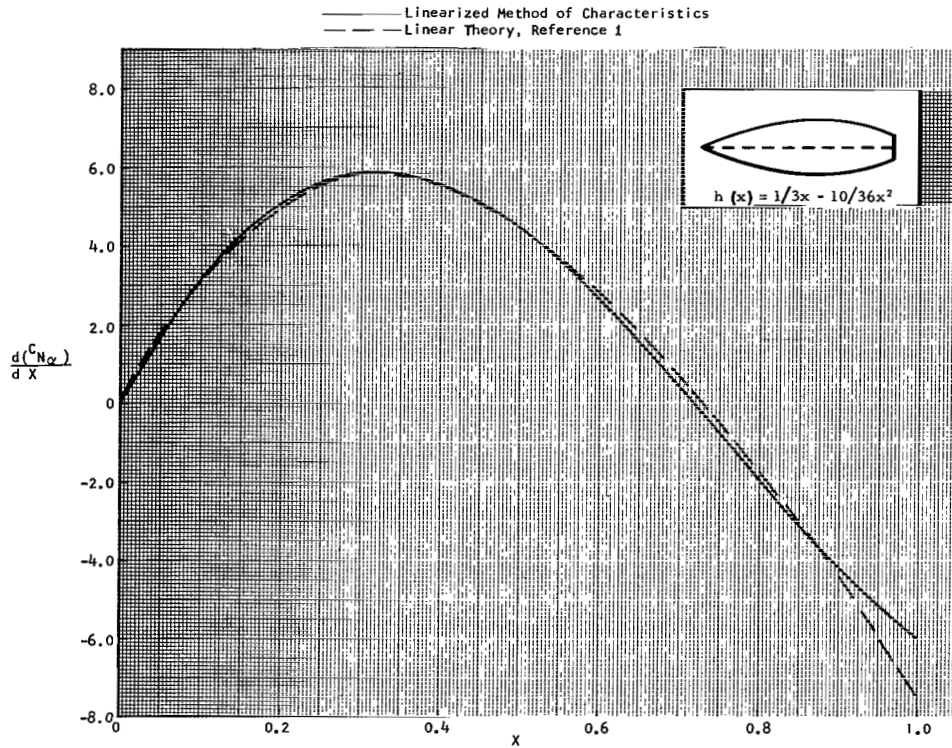OGIVES OF FINENESS RATIO 0.20 AT A MACH NUMBER OF 3.0

FIGURE 40.   LOCAL NORMAL FORCE VARIATION ALONG A BODY CONFIGURATION
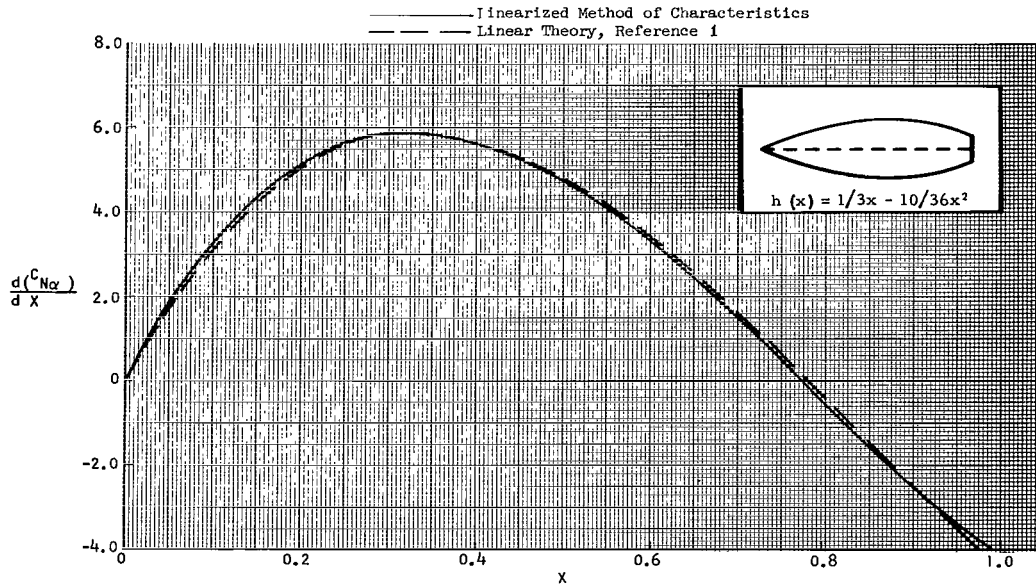DESCRIBED BY THE EQUATION, $h(x) = x/3 - 10x^2/36$, $M_\infty = 1.84$

FIGURE 41. LOCAL NORMAL FORCE VARIATION ALONG A BODY CONFIGURATION DESCRIBED BY THE EQUATION, $h(x) = x/3 - 10x^2/36$, $M_\infty = 2.45$
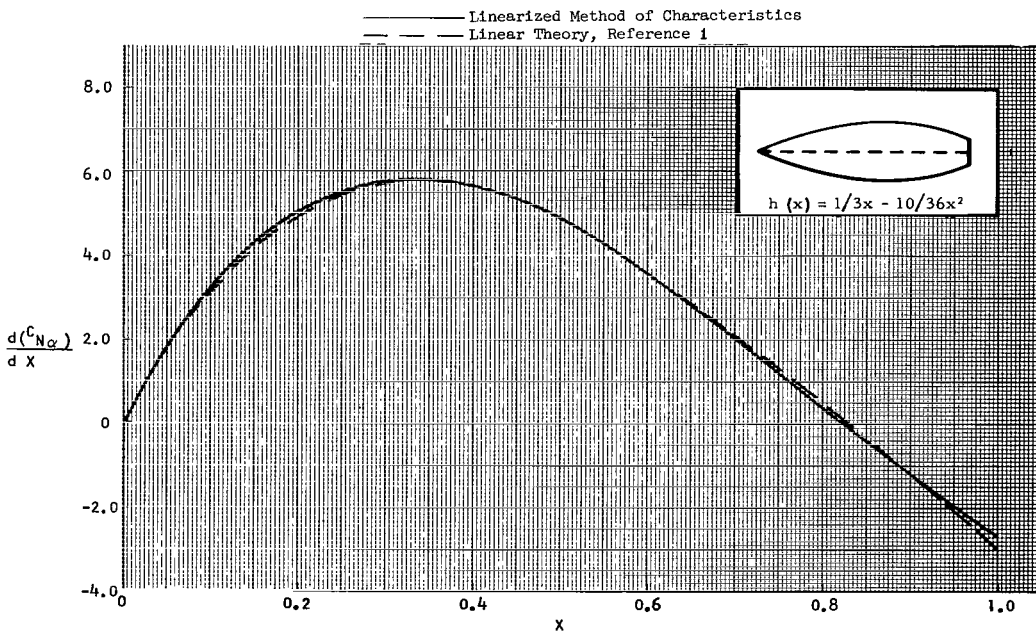

FIGURE 42. LOCAL NORMAL FORCE VARIATION ALONG A BODY CONFIGURATION DESCRIBED BY THE EQUATION, $h(x) = x/3 - 10x^2/36$, $M_\infty = 3.01$

FIGURE 43. COMPARISON BETWEEN THEORY AND EXPERIMENT OF LOCAL NORMAL FORCE VARIATION FOR A CONVEX OGIVE OF FINENESS RATIO 0.066 AT A MACH NUMBER OF 1.59

FIGURE 44. COMPARISON BETWEEN THEORY AND EXPERIMENT OF LOCAL NORMAL FORCE VARIATION FOR A CONVEX OGIVE OF FINENESS RATIO 0.1 AT A MACH NUMBER OF 3.0

$h (x) = 0.10 (2x - x^2)$
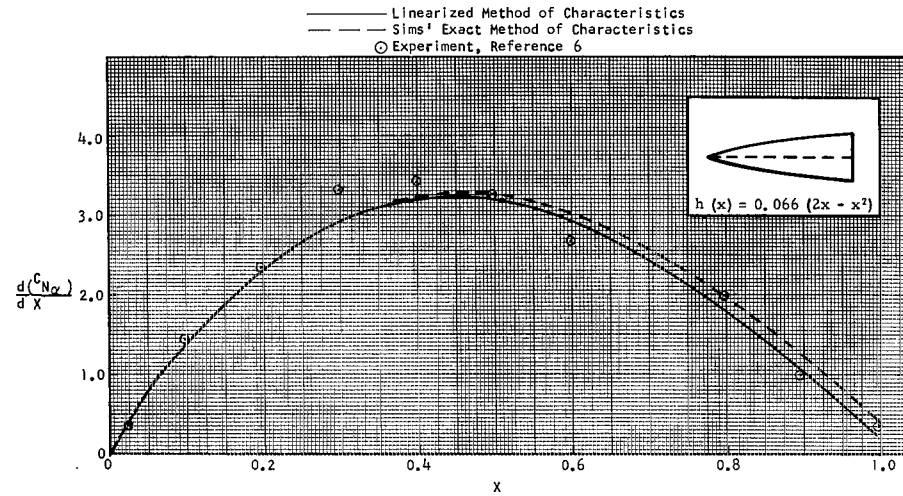
$\dfrac{d\left(^{C}N_{\alpha}\right)}{d\ X}$

X

FIGURE 45.   COMPARISON BETWEEN THEORY AND EXPERIMENT OF LOCAL NORMAL FORCE VARIATION FOR A CONVEX OGIVE OF FINENESS RATIO 0. 1 AT A MACH NUMBER OF 4. 25

$h (x) = 0.1667 (2x - x^2)$

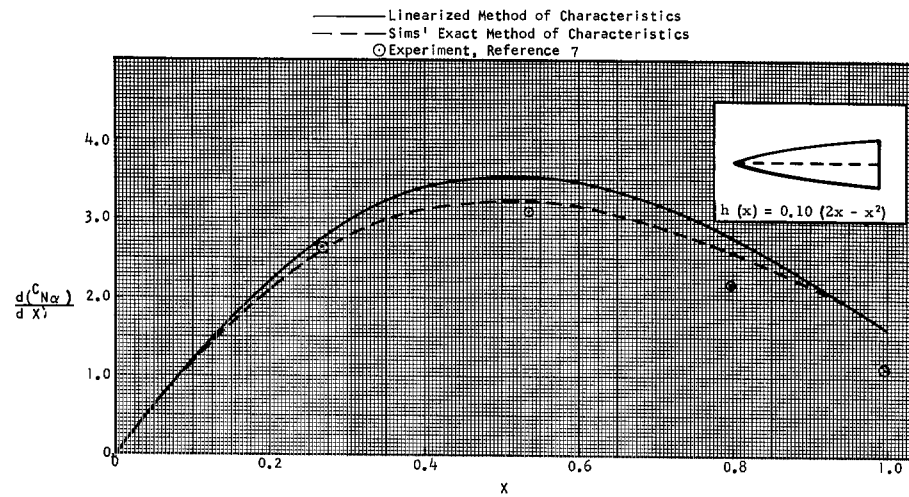$\dfrac{d\left(^{C}N_{\alpha}\right)}{d\ X}$

X

FIGURE 46.   COMPARISON BETWEEN THEORY AND EXPERIMENT OF LOCAL NORMAL FORCE VARIATION FOR A CONVEX OGIVE OF FINENESS RATIO 0. 1667 AT A MACH NUMBER OF 3. 0

37

Linearized Method of Characteristics
Sims' Exact Method of Characteristics
⊙ Experiment, Reference 7

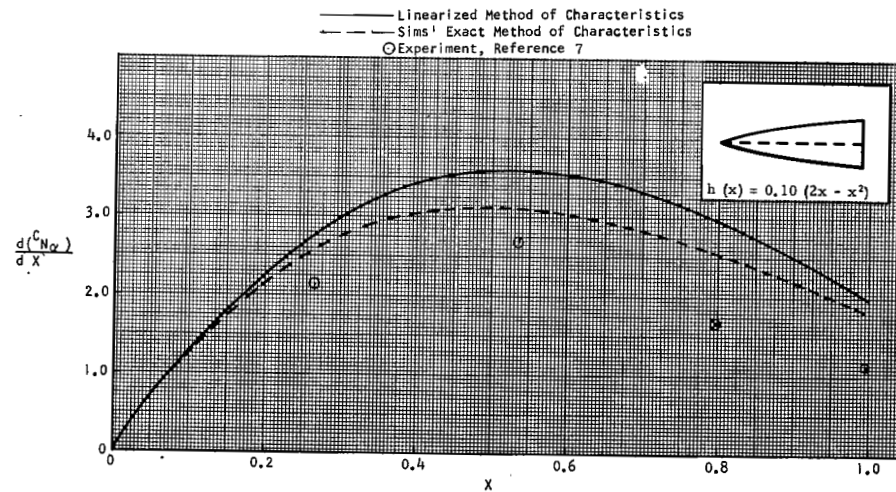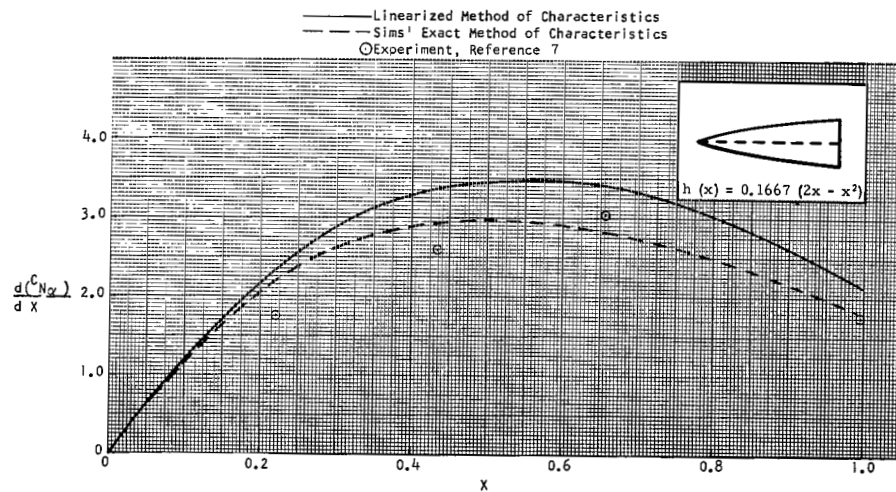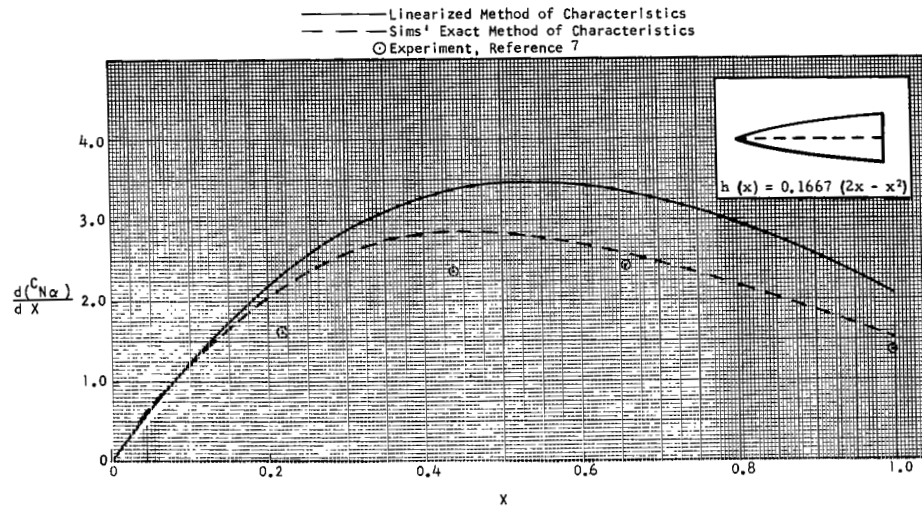$h(x) = 0.1667(2x - x^2)$

$\dfrac{d(C_{N\alpha})}{dX}$

FIGURE 47. COMPARISON BETWEEN THEORY AND EXPERIMENT OF LOCAL NORMAL FORCE
VARIATION FOR A CONVEX OGIVE OF FINENESS RATIO 0.1667 AT A MACH NUMBER OF 4.25

Linearized Method of Characteristics
Sims' Exact Method of Characteristics
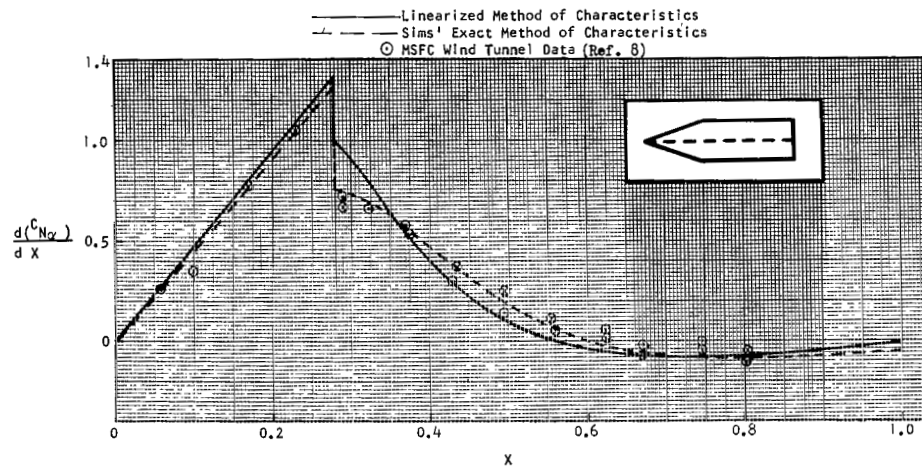⊙ MSFC Wind Tunnel Data (Ref. 8)

$\dfrac{d(C_{N\alpha})}{dX}$

FIGURE 48. LOCAL NORMAL FORCE VARIATION ALONG A 10 DEGREE CONE PLUS
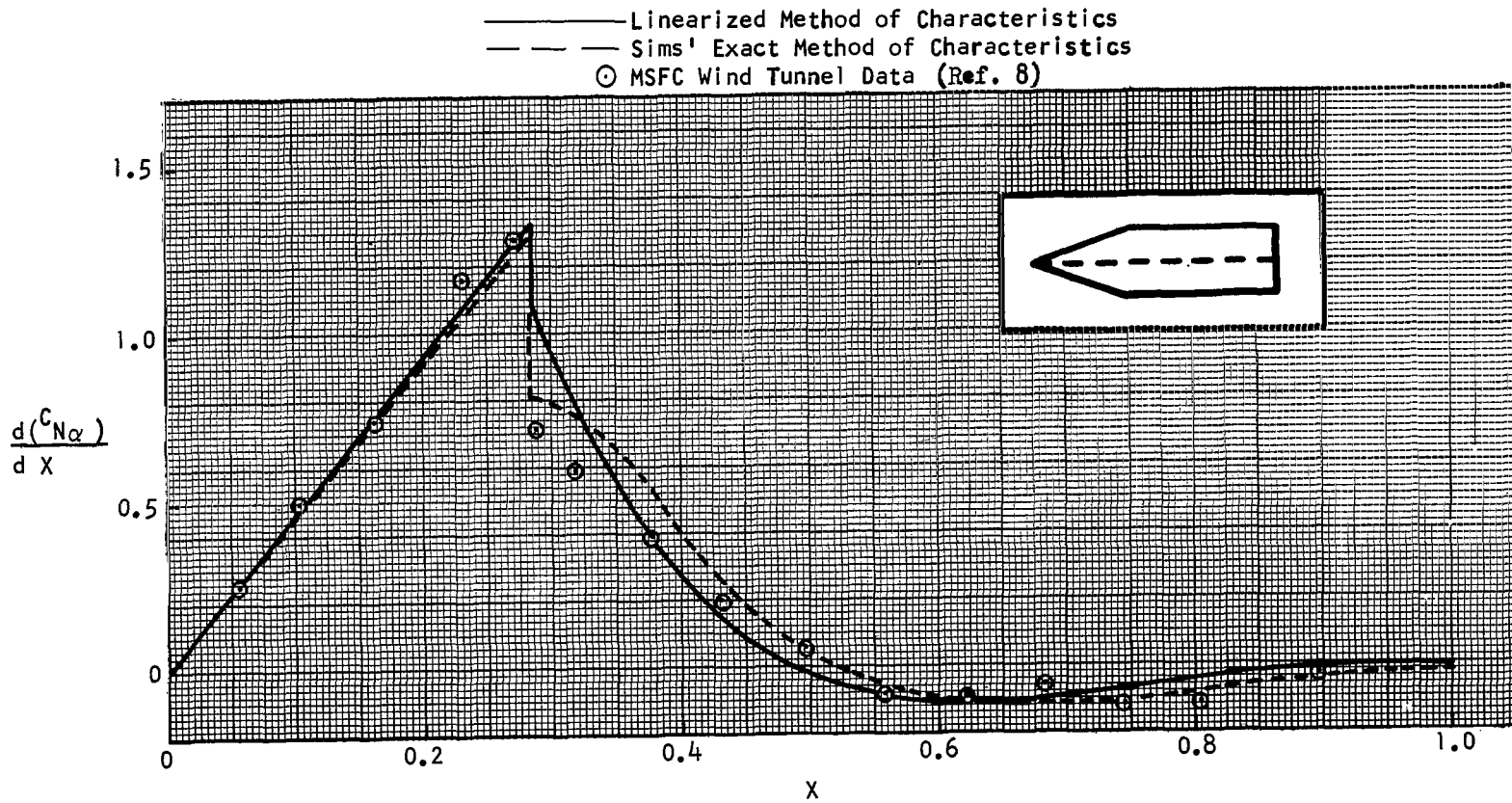CYLINDER BODY, $M_\infty = 1.99$, $\epsilon = .10$

FIGURE 49. LOCAL NORMAL FORCE VARIATION ALONG A 10 DEGREE CONE PLUS
CYLINDER BODY, $M_\infty = 2.44$, $\epsilon = .10$

REFERENCES

1.   Oswatitsch, K.; and Malm, S.: Tryckfordelningsberakningar Pa Tre Rotationskroppar, KTH AERO FL 189, 1955.

2.   Karman, T. V.; and Moore, N. B.: The Resistance of Slender Bodies Moving at Supersonic Velocity with Special Reference to Projectiles. Trans. ASME, vol. 54, 1932.

3.   Tsien, H. S.: Supersonic Flow on an Inclined Body of Revolution. J. Aeron. Sci., vol. 12, 1938.

4.   Oswatitsch, K.; and Erdmann, S. F.: A quick Method of Linear Characteristics for Axial and Oblique Supersonic Flow Around Solids of Revolution with Ring Surfaces. Zeitschroft für Flugwissenschaften, no. 8, 1954, pp. 201-215.

5.   Sears, W. R., et al., ed.: General Theory of High Speed Aerodynamics. Vol. VI. Princeton University Press, 1954.

6.   Cooper, M.; Gapeynski, J. P.; and Hasel, L. E.: A Pressure-Distribution Investigation of a Fineness-Ratio-12.2 Parabolic Body of Revolution (NACA RM-10) at M = 1.59 and Angles of Attack up to 36 Degrees. NACA RM L52G14A, 1952.

7.   Savin, R. C.: Application of the Generalized Shock-Expansion Method to Inclined Bodies of Revolution Traveling at High Supersonic Airspeeds. NACA TN 3349, 1955.

8.   Owens, R. V.: NASA Office Memorandum ORDAB-DAE-8-60. Marshall Space Flight Center, 1960.

NASA SCIENTIFIC AND TECHNICAL PUBLICATIONS

TECHNICAL REPORTS: Scientific and technical information considered important, complete, and a lasting contribution to existing knowledge.

TECHNICAL NOTES: Information less broad in scope but nevertheless of importance as a contribution to existing knowledge.

TECHNICAL MEMORANDUMS: Information receiving limited distribution because of preliminary data, security classification, or other reasons.

CONTRACTOR REPORTS: Technical information generated in connection with a NASA contract or grant and released under NASA auspices.

TECHNICAL TRANSLATIONS: Information published in a foreign language considered to merit NASA distribution in English.

TECHNICAL REPRINTS: Information derived from NASA activities and initially published in the form of journal articles.

SPECIAL PUBLICATIONS: Information derived from or of value to NASA activities but not necessarily reporting the results of individual NASA-programmed scientific efforts. Publications include conference proceedings, monographs, data compilations, handbooks, sourcebooks, and special bibliographies.

Details on the availability of these publications may be obtained from:

SCIENTIFIC AND TECHNICAL INFORMATION DIVISION

NATIONAL AERONAUTICS AND SPACE ADMINISTRATION

Washington, D.C. 20546